This manuscript is a non-peer reviewed manuscript submitted to EarthArXiv.
This manuscript is under review for publication in Journal of Atmospheric and Oceanic Technology.
Copyright in this Work may be transferred without further notice.
Generated using the official AMS LaTeX template v6.1

An improved methodology to estimate cross-scale kinetic energy transfers from third-order structure functions using regularized least-squares

Manuel O. Gutierrez-Villanueva,[a,b] Bruce D. Cornuelle,[a] Sarah T. Gille,[a] Matthew R. Mazloff,[a] Dhruv Balwada,[b]

[a] *Scripps Institution of Oceanography, University of California San Diego, La Jolla, CA*

[b] *Lamont-Doherty Earth Observatory, Columbia University, Palisades, NY*

Corresponding author: Manuel O. Gutierrez-Villanueva, mog002@ucsd.edu

This manuscript is a non-peer reviewed manuscript submitted to EarthArXiv.
This manuscript is under review for publication in Journal of Atmospheric and Oceanic Technology.
Copyright in this Work may be transferred without further notice.

ABSTRACT: Several methods exist for estimating cross-scale kinetic energy (KE) transfers; however, they are ill-adapted for sparse ocean observations, hindering the study of oceanic KE transfers. A newly developed third-order structure function $D3(r)$ framework allows estimation of KE injection rates $\epsilon_j(k)$ and KE transfers $F(k)$ across scales using sparse data. This approach requires inverse methods to convert between separation r and wavenumber k space. A previous study employed the $D3(r)$ framework to estimate $F(k)$ and $\epsilon_j(k)$ using non-negative least squares (NNLS), assuming that $F(k)$ is an increasing function of k, an assumption not always satisfied. In this study, an improved methodology is presented to estimate $F(k)$ and ϵ_j using regularized least-squares (RLS), where the inclusion of prior uncertainty in $D3(r)$ and ϵ_j reduces overfitting. Moreover, the improved methodology allows for estimating both positive and negative ϵ_j and makes no assumptions about the shape of $F(k)$. RLS quantitatively diagnoses the structure of $F(k)$ in an isotropic quasi-geostrophic turbulence simulation, including both positive and negative $\epsilon_j(k)$, an aspect unattainable with NNLS. This improved methodology is also applied to data from two drifter experiments in the Gulf of Mexico. The analysis reveals the presence of bi-directional energy transfers, with a KE inverse cascade at mesoscales in both seasons and a forward cascade at submesoscales that is stronger in winter than summer. Unlike NNLS, RLS fits $D3(r)$ better as the method detects wavenumbers where $\epsilon_j < 0$. This improved methodology allows for a more refined analysis of KE transfers from sparse observations.

This manuscript is a non-peer reviewed manuscript submitted to EarthArXiv.
This manuscript is under review for publication in Journal of Atmospheric and Oceanic Technology.
Copyright in this Work may be transferred without further notice.

1. Introduction

Cross-scale kinetic energy (KE) transfers play a key role in several aspects of ocean circulation (Ferrari and Wunsch 2009), as they mediate the transfer of energy between the scales where the energy is injected into the ocean from the atmosphere and tides, and the scales where it is dissipated by molecular viscosity. Quasi-geostrophic turbulence theory suggests that at mesoscales, O(50-200) km, energy is transferred on average toward larger scales (inverse cascade), and satellite observations provide strong evidence to support this (Scott and Wang 2005; Vallis 2017). Recently, a new body of numerical and observational work has suggested that energy at submesoscales O(1-10) km may be transferred downscale (forward cascade) en route to dissipation (Schubert et al. 2020; Balwada et al. 2022; Freilich et al. 2023; Tedesco et al. 2024). It has also been suggested that mesoscale and submesoscale flows interact by exchanging energy (Sasaki et al. 2017; Steinberg et al. 2022) and that these interactions may help redistribute heat, carbon, and other tracers in the global ocean, with important consequences for global climate (Balwada et al. 2021; Zhang et al. 2023).

Several methods exist to study the energy transfer across scales when gridded data from numerical simulations or mapped observations are available. The most common are spectral methods, which have traditionally been used for estimating KE transfers from gridded velocity fields by considering the Fourier transform in wavenumber space (e.g. Capet et al. 2008; Ajayi et al. 2021; Dong et al. 2020). In addition to requiring uniformly gridded data, spectral methods also require that data be preprocessed by removing spatiotemporal means and windowing to minimize edge effects in nonperiodic domains, which can quantitatively and qualitatively impact the estimated transfer (Aluie et al. 2018). Also, the estimated transfers are obtained as bulk or non-local estimates over the entire study domain, and localized details cannot be inferred. Using wavelets instead of Fourier transforms allows local properties to be probed but still requires similar pre-processing (Uchida et al. 2023). More recently, a coarse-graining approach has been introduced in oceanography (Aluie et al. 2018), which parses flow at different scales with the help of filtering (e.g., top-hat filter). This method also requires gridded data but has the advantage of estimating the cross-scale transfers at each location, similar to wavelets, and does not require data to be artificially made periodic (Aluie et al. 2018; Srinivasan et al. 2023; Freilich et al. 2023; Naveira Garabato et al. 2022; Tedesco et al. 2024; Schubert et al. 2023, 2020; Storer et al. 2023). Since all these approaches

This manuscript is a non-peer reviewed manuscript submitted to EarthArXiv.
This manuscript is under review for publication in Journal of Atmospheric and Oceanic Technology.
Copyright in this Work may be transferred without further notice.

require gridded data, they are technically challenging to implement with sparse or non-uniformly sampled observations, impeding their use to study KE transfers in the real ocean.

An alternative to relying on gridded information for estimating kinetic energy (KE) transfers involves using third-order velocity structure functions. Third-order structure functions are foundational for three-dimensional turbulence theory (Kolmogorov 1991), which predicts that when KE cascades downscale at a rate of ϵ in the inertial range, the third-order structure function takes the exact form $\delta u_L^3(r) = -(4/5)\epsilon r$, where r is the two-point separation distance and δu_L is the longitudinal third-order structure function. Although this exact law is unlikely to hold in more complex, realistic scenarios, the sign of the third-order structure function has been widely employed as a heuristic tool to infer the direction of energy transfer in studies of natural flows (Lindborg 1999; Lindborg and Cho 2001; Cho and Lindborg 2001; Qiu et al. 2022; Balwada et al. 2016; Poje et al. 2017). However, this heuristic approach faces limitations due to challenges in identifying inertial ranges in oceanic flows and determining the turbulence regime (e.g., 2D, 3D, or quasi-geostrophic). These uncertainties undermine the robustness of ϵ estimates when the underlying assumptions are violated.

A recently developed framework by Xie and Bühler (2019) employs third-order structure functions to estimate energy injection rates across multiple forcing scales and to resolve bi-directional KE transfers. The new framework does not require identifying inertial ranges and can be applied to scattered and heterogeneous data under assumptions of axisymmetry (isotropy) and homogeneity. Balwada et al. (2022) implemented this methodology using a piecewise constant transfer basis to identify multiple forcing scales in KE transfers, using two drifter datasets collected in summer and winter that resolve submesoscale flows down to $O(100)$ m. They employed a non-negative least-squares (NNLS) method to invert the third-order structure functions and estimate KE injection rates. However, the NNLS method inherently cannot capture negative KE injection rates (indicative of KE transfer convergence). As a result, the derived KE transfers are strictly increasing with wavenumber — an assumption that may not hold universally, such as during the conversion of KE to potential energy.

Here, we improve on the estimation of the KE transfers presented by Balwada et al. (2022) by utilizing regularized least-squares (RLS) (e.g. Wunsch 1996; Kachelein et al. 2022). The RLS approach allows us to 1) prescribe a prior uncertainty in the KE injection rates, reducing

This manuscript is a non-peer reviewed manuscript submitted to EarthArXiv.
This manuscript is under review for publication in Journal of Atmospheric and Oceanic Technology.
Copyright in this Work may be transferred without further notice.

overfitting in the inversion problem that leads to non-physical energy transfers when using ordinary least-squares, 2) propagate the uncertainty in the estimated third-order structure functions to the calculated KE transfers and injection rates, 3) make no assumptions regarding the direction of the KE transfers, and thus 4) potentially identify energy sinks. The RLS fits assumes that errors in the structure function and fitted parameters are Gaussian-distributed.

To demonstrate the success of RLS in estimating KE transfers, we first use an idealized two-layer quasi-geostrophic (QG) model (Abernathey et al. 2022) that generates isotropic mesoscale eddies. In this scenario, energy is injected into the flow near the baroclinic deformation radius, transferred to the larger-scale flows, and dissipated at larger scales through bottom drag. We show that the RLS method resolves the expected shape of the KE transfers as it resolves KE sinks (negative KE injection rates) that are otherwise unresolved by the NNLS method, as the latter is incapable of estimating negative injection rates. We then apply this methodology to drifter data from two targeted experiments in the Gulf of Mexico (Balwada et al. 2022), improving the estimates of the bi-directional cascade and its seasonality. The results confirm an inverse cascade at mesoscales and a forward cascade at submesoscales, modulated by seasonal energy injection. Unlike NNLS, RLS is capable of fitting $D3(r)$ better and detecting wavenumbers with negative ϵ_j. The paper is organized as follows: Section 2 reviews the structure-function and KE transfers theory. The improved methodology is explained in section 3. Details of the model setup, the drifter data, and the steps to estimate structure functions are presented in section 4. Results from the QG model are presented in Section 5a, while Section 5b explores drifter experiments and compares estimates with prior studies. Also, Section 5 presents sample distributions of the third-order structure function, along with the steps taken to estimate prior uncertainties in both the structure function and injection rates. Section 6 concludes with a summary of the improved methodology's results, advantages, and limitations.

2. Structure Function Framework

Structure functions provide a powerful framework for diagnosing ocean energetics from sparse observations. The foundation of this approach is the estimation of two-point differences in scalars

This manuscript is a non-peer reviewed manuscript submitted to EarthArXiv.
This manuscript is under review for publication in Journal of Atmospheric and Oceanic Technology.
Copyright in this Work may be transferred without further notice.

or vectors, such as velocity differences:

$$\delta\mathbf{u}(\mathbf{s},\mathbf{r},t) = \mathbf{u}(\mathbf{s}+\mathbf{r},t) - \mathbf{u}(\mathbf{s},t), \tag{1}$$

where $\delta\mathbf{u}$ represents the velocity difference between two points $\mathbf{s}$ and $\mathbf{s}+\mathbf{r}$ separated by the vector $\mathbf{r}$ at time t. These velocity differences are the central focus of this study. To avoid reliance on fixed geographical coordinates, we decompose $\delta\mathbf{u}$ into longitudinal and transverse components $\delta\mathbf{u} = (\delta u_L, \delta u_T)$:

$$\delta u_L = \delta\mathbf{u}\cdot\frac{\mathbf{r}}{|\mathbf{r}|}, \quad \delta u_T = \frac{\widehat{\mathbf{z}}\cdot(\delta\mathbf{u}\times\mathbf{r})}{|\mathbf{r}|}, \tag{2}$$

where $\widehat{\mathbf{z}}$ is the vertical unit vector.

a. First- and second-order velocity structure functions

Given a sample set of velocity differences across many random pairs, velocity structure functions are defined as raw statistical moment of these random variables. Here we defined the first-order structure function $D1(r)$ for stationary, homogeneous and isotropic flows as:

$$D1(r) = D1_L(r) + D1_T(r) = \langle\delta u_L(\mathbf{s},\mathbf{r},t)\rangle + \langle\delta u_T(\mathbf{s},\mathbf{r},t)\rangle, \tag{3}$$

where $r = |\mathbf{r}|$, and $\langle\cdot\rangle$ represents the ensemble average over all members of the ensemble at each r. Often, in practice, and when the assumptions of stationary, isotropy, and homogeneity approximately hold, ensemble averaging is replaced by averaging over all samples corresponding to a spatio-temporal average. Also, we chose to define $D1(r)$ as a sum of the longitudinal $D1_L(r)$ and transverse $D1_T(r)$ components, but other choices with different interpretations are also valid. $D1(r)$ provides a measure of the strength of the gradients in the mean flow and is rarely discussed in the theoretical literature that often assumes that the background mean flow is zero or constant.

Similarly, the second-order structure is defined as,

$$D2(r) = D2_{LL}(r) + D2_{TT}(r) = \langle\delta u_L^2(\mathbf{s},\mathbf{r},t)\rangle + \langle\delta u_T^2(\mathbf{s},\mathbf{r},t)\rangle, \tag{4}$$

which is a sum of the longitudinal and transverse components, denoted as $D2_{LL}(r)$ and $D2_{TT}(r)$, respectively. $D2(r)$ provides a measure of the turbulent flow at a certain scale r and can be precisely

This manuscript is a non-peer reviewed manuscript submitted to EarthArXiv.
This manuscript is under review for publication in Journal of Atmospheric and Oceanic Technology.
Copyright in this Work may be transferred without further notice.

connected to the isotropic KE spectrum $E(k)$ as:

$$D2(r) = 2\int_0^\infty E(k)[1 - J_0(kr)]dk, \tag{5}$$

where J_0 is the zeroth-order Bessel function (Bennett 1984), $k = \sqrt{k_x + k_y}$ is the isotropic wavenumber (k_x and k_y are the zonal and meridional wavenumbers, respectively), and dk is the wavenumber resolution. Assuming the existence of a KE spectrum with self-similar form $E(k) \sim k^{-\theta}$, one can show using (5) that the second-order structure function has a form of $D2(r) \sim r^{\theta-1}$ where θ is the wavenumber spectral slope (Bennett 1984).

b. Third-order structure function and cross-scale KE transfers

At the third order, we follow Balwada et al. (2022), employing the theoretical framework of Xie and Bühler (2019), who derived a formulation (from the Karman–Howarth–Monin equation) capable of capturing bi-directional KE transfers by using the calculated isotropic third-order structure function. The third-order structure function, defined as

$$D3(r) = D3_{LLL}(r) + D3_{LTT}(r) = \langle \delta u_L(\mathbf{s},\mathbf{r},t)[\delta u_L^2(\mathbf{s},\mathbf{r},t) + \delta u_T^2(\mathbf{s},\mathbf{r},t)]\rangle, \tag{6}$$

can be referred to as the longitudinal third-order structure function. $D3(r)$ is related to azimuthally averaged 2D cross-scale KE transfers $F(k)$ through the following relationship (i.e., a Hankel transform):

$$D3(r) = -4r\int_0^\infty \frac{1}{k}F(k)J_2(kr)dk, \tag{7}$$

where J_2 is the second-order Bessel function (Xie and Bühler 2019). $F(k) > 0$ indicates a forward cascade (i.e., KE transfer toward smaller scales); conversely, $F(k) < 0$ indicates an inverse cascade (toward larger scales). Assuming periodicity, isotropy, and homogeneity, the spectral transfers are calculated from the KE equation as (e.g., Ajayi et al. 2021; Capet et al. 2008)

$$F_\Pi(k) = -\int_{k_2}^{k_1} \mathrm{Re}\left[\widehat{\mathbf{u}}^* \cdot \widehat{(\mathbf{u}\cdot\nabla\mathbf{u})}\right]dk, \tag{8}$$

This manuscript is a non-peer reviewed manuscript submitted to EarthArXiv.
This manuscript is under review for publication in Journal of Atmospheric and Oceanic Technology.
Copyright in this Work may be transferred without further notice.

where $\widehat{()}$ indicates a Fourier transform, $\widehat{()}^*$ is the complex conjugate, and $\nabla = (\partial_x, \partial_y)$ is the horizontal velocity gradient operator (∂_x, ∂_y).

Balwada et al. (2022) suggest that a convenient way to discretize the spectral flux is by using a basis formed by step functions as

$$F(k) = -\epsilon_u + \sum_{j=1}^{N_k} \epsilon_j H(k - k_j) dk_j, \tag{9}$$

where ϵ_u is the upscale KE injection and $\epsilon_j dk_j = \epsilon_u + \epsilon_d$ is the total KE injection ($\epsilon_d > 0$ is the downscale energy transfer), H is the Heaviside function and N_k represents the number of discrete wavenumbers chosen. Substituting (9) in (7) yields

$$D3(r) = 2\epsilon_u r - \sum_{j=1}^{N_k} 4 \frac{\epsilon_j}{k_j} J_1(k_j r) dk_j. \tag{10}$$

This equation provides the starting point for a discrete linear inverse problem, where the goal is to estimate ϵ_u and ϵ_j at a selected range of k_j from an estimated $D3(r)$. The following section describes the inverse problem and the regularized least-squares fitting employed to estimate the KE injection rates and transfers.

3. Regularized Least Squares

We use a least-squares approach to solve the linear problem, writing (10) as a matrix equation:

$$\mathbf{y} = \mathbf{H}\mathbf{x} + \mathbf{e}, \tag{11}$$

where $\mathbf{x}$ is the column vector of size $M \times 1$ (where $M = N_k + 1$) representing the unknown parameters (ϵ_u and ϵ_js), $\mathbf{y}$ is the vector of data to fit (i.e., $D3(r)$) of size N_r (number of discrete r bins), $\mathbf{e}$ is

This manuscript is a non-peer reviewed manuscript submitted to EarthArXiv.
This manuscript is under review for publication in Journal of Atmospheric and Oceanic Technology.
Copyright in this Work may be transferred without further notice.

the residual, and $\mathbf{H}$ is the model matrix formulated from (10) of size $N_r \times M$ defined as:

$$\mathbf{H} = \begin{bmatrix} 2r_1 & -4\frac{dk}{k_1}J_1(r_1k_1) & -4\frac{dk}{k_2}J_1(r_1k_2) & -4\frac{dk}{k_3}J_1(r_1k_3) & \cdots & -4\frac{dk}{k_{N_k}}J_1(r_1k_{N_k}) \\ 2r_2 & -4\frac{dk}{k_1}J_1(r_2k_1) & -4\frac{dk}{k_2}J_1(r_2k_2) & -4\frac{dk}{k_3}J_1(r_2k_3) & \cdots & -4\frac{dk}{k_{N_k}}J_1(r_2k_{N_k}) \\ 2r_3 & -4\frac{dk}{k_1}J_1(r_3k_1) & -4\frac{dk}{k_2}J_1(r_3k_2) & -4\frac{dk}{k_3}J_1(r_3k_3) & \cdots & -4\frac{dk}{k_{N_k}}J_1(r_3k_{N_k}) \\ \vdots & \vdots & \vdots & \vdots & \ddots & \vdots \\ 2r_{N_r} & -4\frac{dk}{k_1}J_1(r_{N_r}k_1) & -4\frac{dk}{k_2}J_1(r_{N_r}k_2) & -4\frac{dk}{k_3}J_1(r_{N_r}k_3) & \cdots & -4\frac{dk}{k_{N_k}}J_1(r_{N_r}k_{N_k}) \end{bmatrix}. \quad (12)$$

Here, we used the Fourier wavenumber definition $k = k_0, \ldots, k_{N_k}$, where $k_0 = 1/r_{N_r}$, k_{N_k} is the Nyquist wavenumber, and $dk_j = k_0$.

The ordinary least-squares method is ill-suited for this problem since the method can overfit data as the size of the fitted parameters is unconstrained when minimizing the mean square error $\mathbf{e}^2 = ||\mathbf{Hx} - \mathbf{y}||_2^2$, even when weighted using the data prior uncertainty. This results in non-physical injection rates and energy transfers (see Supplementary Information in Balwada et al. 2022). To overcome this limitation, Balwada et al. (2022) constrained their least-squares method by assuming that energy injection rates ϵ_j were always non-negative, which is equivalent to assuming that $F(k)$ is purely an increasing function of k.

RLS fitting permits convergence of KE transfers ($\epsilon_j < 0$) without assuming a direction of the KE transfers, to determine posterior uncertainty for the fitted parameters, and to identify more accurately the scale that best marks the transition between upscale and downscale cascades. An advantage of RLS is that it reduces overfitting (with some bias in our estimated parameters) by choosing a constraint with prior knowledge of the expected values. Additionally, RLS fitting is applicable for both under-determined and over-determined systems. RLS requires that the terms in (11), $\mathbf{x}$ and $\mathbf{e}$, have Gaussian distributions.

If these distributions are Gaussian, then following Kachelein et al. (2022) and Wunsch (1996), the most probable model solutions are given by

$$\widetilde{\mathbf{x}} = \left(\mathbf{H}^{\mathrm{T}}\mathbf{W}^{-1}\mathbf{H} + \mathbf{P}^{-1}\right)^{-1}\mathbf{H}^{\mathrm{T}}\mathbf{W}^{-1}\mathbf{y}, \quad (13)$$

where $\mathbf{W} = \langle \mathbf{e}\mathbf{e}^{\mathrm{T}} \rangle$ is the data covariance matrix representing the prior data uncertainty and is of size $N_r \times N_r$; $\mathbf{P} = \langle \mathbf{x}\mathbf{x}^{\mathrm{T}} \rangle$ is the covariance matrix representing the prior uncertainty of the fitted

This manuscript is a non-peer reviewed manuscript submitted to EarthArXiv.
This manuscript is under review for publication in Journal of Atmospheric and Oceanic Technology.
Copyright in this Work may be transferred without further notice.

parameters and is $M \times M$ (Kachelein et al. 2022; Wunsch 1996). As a practical convenience, $\mathbf{W}$ and $\mathbf{P}$ are defined to be diagonal matrixes with off-diagonal entries of zero and with the diagonals set to the squared uncertainty of $D3(r)$ and ϵ_u, ϵ_j, respectively. We can recover the ordinary least-squares solution in (13) by setting the elements on the diagonal of $\mathbf{W}$ to 1 and letting $\mathbf{P}^{-1} \to 0$. The addition of $\mathbf{P}$ in (13) constrains the size of the solution $\mathbf{x}$, preventing it from straying too far from our prior knowledge. This allows for independent solutions even when $\mathbf{H}$ is rank deficient.

We can gain knowledge of the statistics of the differences between the expected true and estimated parameters from the posterior uncertainty covariance matrix

$$\mathbf{C_{xx}} = \left\langle (\mathbf{x} - \widetilde{\mathbf{x}})(\mathbf{x} - \widetilde{\mathbf{x}})^{\mathrm{T}} \right\rangle = \left(\mathbf{H}^{\mathrm{T}}\mathbf{W}^{-1}\mathbf{H} + \mathbf{P}^{-1}\right)^{-1}, \tag{14}$$

where the diagonal of (14) represents the squared uncertainty of ϵ_u, ϵ_j. Equation (13) is analogous to the ridge regression equation presented by Wunsch (1996). We transform the uncertainty in ϵ_j and ϵ_u in (14) to uncertainty in transfers $F(k)$ as

$$\mathbf{F_{xx}} = \left\langle (\mathbf{Gx})(\mathbf{Gx})^{\mathrm{T}} \right\rangle = \mathbf{G}\mathbf{C_{xx}}\mathbf{G}^{\mathrm{T}}, \tag{15}$$

where $\mathbf{G}$ is the $M \times M$ transformation matrix formulated with (9):

$$\mathbf{G} = \begin{bmatrix} -1 & H(k_1 - k_1)dk & H(k_1 - k_2)dk & H(k_1 - k_3)dk & \cdots & H(k_1 - k_{N_k})dk \\ -1 & H(k_2 - k_1)dk & H(k_2 - k_2)dk & H(k_2 - k_3)dk & \cdots & H(k_2 - k_{N_k})dk \\ -1 & H(k_3 - k_1)dk & H(k_3 - k_2)dk & H(k_3 - k_3)dk & \cdots & H(k_3 - k_{N_k})dk \\ \vdots & \vdots & \vdots & \vdots & \ddots & \vdots \\ -1 & H(k_{N_k} - k_1)dk & H(k_{N_k} - k_2)dk & H(k_{N_k} - k_3)dk & \cdots & H(k_{N_k} - k_{N_k})dk \end{bmatrix}, \tag{16}$$

where the diagonal of (16) represents the squared uncertainty of $F(k)$. The off-diagonal elements represent correlated uncertainty.

4. Datasets and Methodological Details

In this study, we show that the RLS technique is capable of estimating the shape and magnitude of the KE transfers by applying it to a two-layer QG turbulence model output where the dynamics and energetics are known. After demonstrating the utility of the improved methodology, we apply

This manuscript is a non-peer reviewed manuscript submitted to EarthArXiv.
This manuscript is under review for publication in Journal of Atmospheric and Oceanic Technology.
Copyright in this Work may be transferred without further notice.

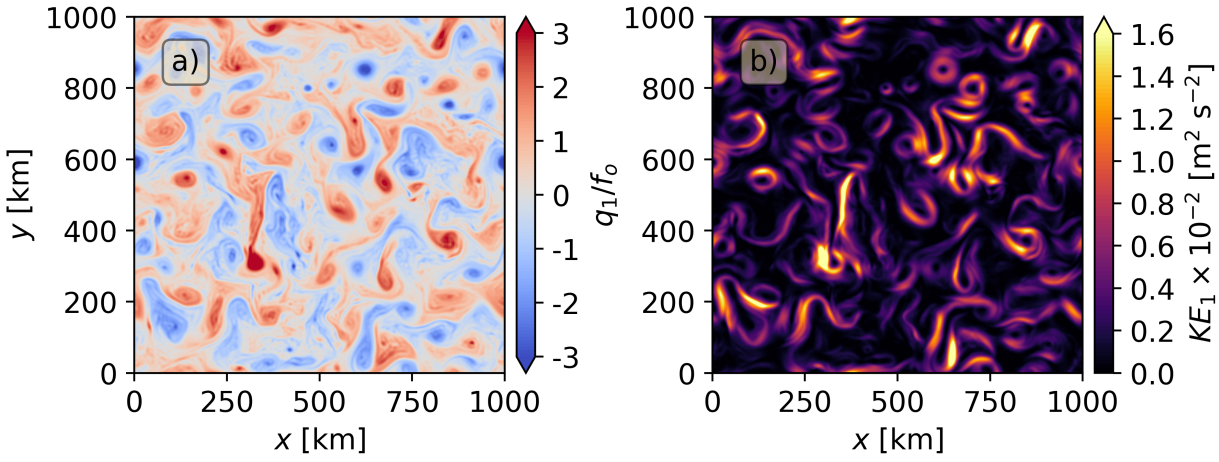

FIG. 1. Daily-averaged (a) Coriolis-normalized QG potential vorticity q_1/f_o and (b) KE_1 [m^2 s^{-2}] from the isotropic two-layer QG model for $t = 6$ year.

it to drifter observations from two targeted experiments in the Gulf of Mexico. These two datasets and the steps taken to estimate the structure functions are described in this section.

1) TWO-LAYER QG MODEL

A horizontal velocity field (u, v) using a two-layer QG model (PyQG; Abernathey et al. 2022) (see details in Appendix A) was simulated to test whether the RLS methodology can quantify all the details of the spectral transfers.

The model configuration is similar to the high-resolution eddy configuration of Ross et al. (2023), which generates a field of isotropic eddies (Fig. 1). The configuration is a flat bottom doubly periodic square domain of size $L_x = L_y = 1000$ km, with $n_x = n_y = 256$ corresponding to a uniform grid spacing of ~ 3.9 km. The simulation is forced with a mean vertical shear, set by $U_1 = 0.025$ m s^{-1} and $U_2 = 0$ in the top and bottom layer of mean thicknesses $H_1 = 500$ m and $H_2 = 2000$ m. Layer densities are chosen such that the Rossby radius $r_d = 15$ km (characteristic of high-latitude environments), which is large enough to be well resolved on the chosen grid. Also, $\beta = 1.5 \times 10^{-11}$ m^{-1} s^{-1}, and bottom drag is $r_{ek} = 5.787 \times 10^{-7}$ s^{-1}. The model is spun up for five years and run for 15 years with a time step of 1 hr. For computational convenience, we saved and used daily averaged horizontal velocity fields. We only used the model's upper layer.

This manuscript is a non-peer reviewed manuscript submitted to EarthArXiv.
This manuscript is under review for publication in Journal of Atmospheric and Oceanic Technology.
Copyright in this Work may be transferred without further notice.

Velocity differences $\delta\mathbf{u}$ (1) were calculated for unique grid-point pairs for each daily step. These velocity differences were then rotated to form longitudinal δu_L and transverse δu_T components (2), which were then binned into equally spaced r bins spanning between 1 km and 230 km with a bin size of 4 km (i.e., $\sim \Delta x$). Since we also formed pairs in directions that are not aligned with the grid, e.g., along diagonals, the average separation between averaged r in each bin is ~ 5.5 km. Also, assuming isotropy, we only kept track of pair separation and not the pair orientation. This data from binned pairs forms the samples/random variables, whose moments can be calculated to obtain the structure functions at different orders.

2) Drifter data

We used data from two targeted drifter releases in the northeastern Gulf of Mexico, also used by Balwada et al. (2022). The Grand Lagrangian Deployment (GLAD) experiment released 300 drifters during summer (July-September 2012), and the Lagrangian Submesoscale Experiment (LASER) released approximately 1000 drifters during winter (January-March 2015). These GPS-tracked drifters reported positions at 5-min intervals (position error < 10 m), which were subsequently low-pass filtered with a 1-hour cutoff and sub-sampled to 15 min. Following Balwada et al. (2022), we used a subset of the drifter dataset shown in Fig. 2 in waters deeper than 500 m.

To calculate structure functions for this drifter data, we followed Balwada et al. (2022). First, velocity differences (5) were calculated for all possible unique pairs of drifters at every time for each drifter dataset. These velocity differences were then decomposed into δu_L and δu_T and binned into r bins for all orientations, collecting pairs of overall time sampled by each experiment. Here, the r bins were defined to be logarithmically distributed for 10^1 m $\leq r \leq 10^6$ m as $r_a = r_0 \times 1.5^a$, where $r_0 = 10$ m and $a = (0, 1, 2, 3, ...)$. These data from binned pairs form the samples/random variables, whose raw moments can be calculated to obtain the structure functions at different orders.

5. Results

Here, we present the results of applying RLS to the velocity fields from the QG simulation, followed by its application to drifter observations in the Gulf of Mexico. We also thoroughly discuss how uncertainties may be estimated and compare RLS-derived results against other approaches when possible.

This manuscript is a non-peer reviewed manuscript submitted to EarthArXiv.
This manuscript is under review for publication in Journal of Atmospheric and Oceanic Technology.
Copyright in this Work may be transferred without further notice.

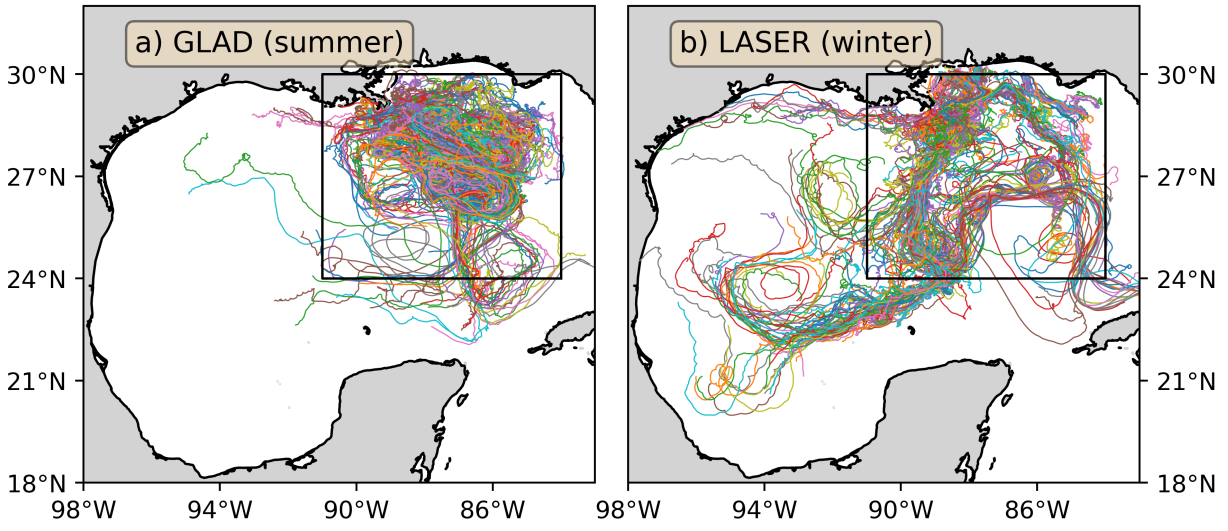

FIG. 2. Drifter trajectories from the (a) GLAD (summer) and (b) LASER (winter) experiments. Each color represents a drifter trajectory. In each panel, the box shows the subset of data used in this analysis and by Balwada et al. (2022).

a. Two-Layer Quasi-Geostrophic Turbulence

In two-layer QG turbulence, the flow is stirred, or energy is injected into the flow, by baroclinic instability around the deformation radius r_d. Similar to 2D turbulence, we expect an inverse cascade of energy (and a forward cascade of enstrophy) in each layer. At scales larger than the deformation radius, the flow becomes more barotropic, and thus some of the energy cascading to larger scales in the top layer will be transferred to the lower layer. Our goal in this subsection is to show that, unlike NNLS, the RLS is capable of estimating the details of these properties, as expected in QG turbulence.

1) SAMPLES AND UNCERTAINTY OF THIRD-ORDER STRUCTURE FUNCTION

An important assumption for RLS to work is that the prior errors $\mathbf{e}$ are Gaussian-distributed (Wunsch 1996; Kachelein et al. 2022). In this subsection, we examine the distribution of the samples of $D3(r)$ to determine if the errors in $D3(r)$ are Gaussian distributed.

The third-order structure function $D3(r)$ is an ensemble mean of $\delta u3(\mathbf{s},\mathbf{r},t) = \delta u_L(\mathbf{s},\mathbf{r},t)[\delta u_L^2(\mathbf{s},\mathbf{r},t) + \delta u_T^2(\mathbf{s},\mathbf{r},t)]$ over many pair samples coming from different locations, orientations, and times. The distribution of $\delta u3(\mathbf{s},\mathbf{r},t)$ is shown as a function of time at two

This manuscript is a non-peer reviewed manuscript submitted to EarthArXiv.
This manuscript is under review for publication in Journal of Atmospheric and Oceanic Technology.
Copyright in this Work may be transferred without further notice.

different separations (~ 43 and ~ 82 km) in Fig. 3. For convenience, we only show the first of the five years. The $\delta u3$ distributions are non-Gaussian (i.e., very heavy-tailed and slightly skewed) and fluctuate in time, with events reaching many standard deviations away from the mean. These intermittent events reach nearly $5-10$ at ~ 43 km and $10-20$ standard deviations at ~ 82 km. These extreme events play a role in setting the mean, and thus $D3(r)$. We conclude that the samples of the third-order structure function are non-Gaussian distributed, which breaks the RLS's requirement for Gaussian-distributed errors. Consequently, we look for an alternative avenue to construct Gaussian-distributed samples and errors in $D3(r)$.

To construct Gaussian-distributed samples, we average $\delta u3(\mathbf{s},\mathbf{r},t)$ over the full spatial domain and all orientations of $\mathbf{r}$ ($\bar{\cdot}$), and without any temporal average. These samples are denoted by $\overline{\delta u3}(r,t)$. Averaging $\delta u3(\mathbf{r},\mathbf{s},t)$ over all orientations and positions results in Gaussian-distributed sample means $\overline{\delta u3}(r,t)$ at each r per the central limit theorem (Stroock 2010). To confirm that $\overline{\delta u3}(r,t)$ is Gaussian distributed, we show PDFs of $\overline{\delta u3}(r,t)$ normalized by the standard deviation of the means over time $\sigma_{\overline{\delta u3}}$ at two separations as examples (Fig. 4a). Visually, these PDFs show that the distribution of sample means is close to Gaussian, confirmed by good agreement with the expected Gaussian distribution (dashed). In contrast to the raw samples $\delta u3(\mathbf{s},\mathbf{r},t)$ (Fig. 3), the means and tails of $\overline{\delta u3}(r,t)$ fall within three to four standard deviations (Fig. 4a). Also, the estimated skewness and excess kurtosis at each r are lightly positively skewed, with no long tails (excess kurtosis < 1; Fig. 4b). Thus, the $\overline{\delta u3}(r,t)$ is Gaussian distributed and fulfills the RLS requirement that $\mathbf{e}$ have a Gaussian distribution.

2) Regularized least-squares fitting and KE transfers

The isotropic energy spectrum $E(k)$ (see Appendix B) from the simulation shows that eddies with scales $\sim$100 km are the largest source of KE. The spectrum follows a steep $\sim k^{-4}$ power law, which might be indicative of an inverse energy cascade (forward enstrophy cascade). However, the spectrum lacks detailed information on the shape and magnitude of the energy transfers. Thus, we proceed with the inversion problem using RLS to recover a trustworthy estimate of $F(k)$ from a given $D3(r)$. The five-year $D3(r)$ is estimated here by ensemble averaging $\overline{\delta u3}(r,t)$. We notice it would be hard to estimate the ensemble mean $D3(r)$ from samples obtained from a short sampling period (gray solid, Fig. 5a). Moreover, we show that RLS fitting is capable of capturing the shape

This manuscript is a non-peer reviewed manuscript submitted to EarthArXiv.
This manuscript is under review for publication in Journal of Atmospheric and Oceanic Technology.
Copyright in this Work may be transferred without further notice.

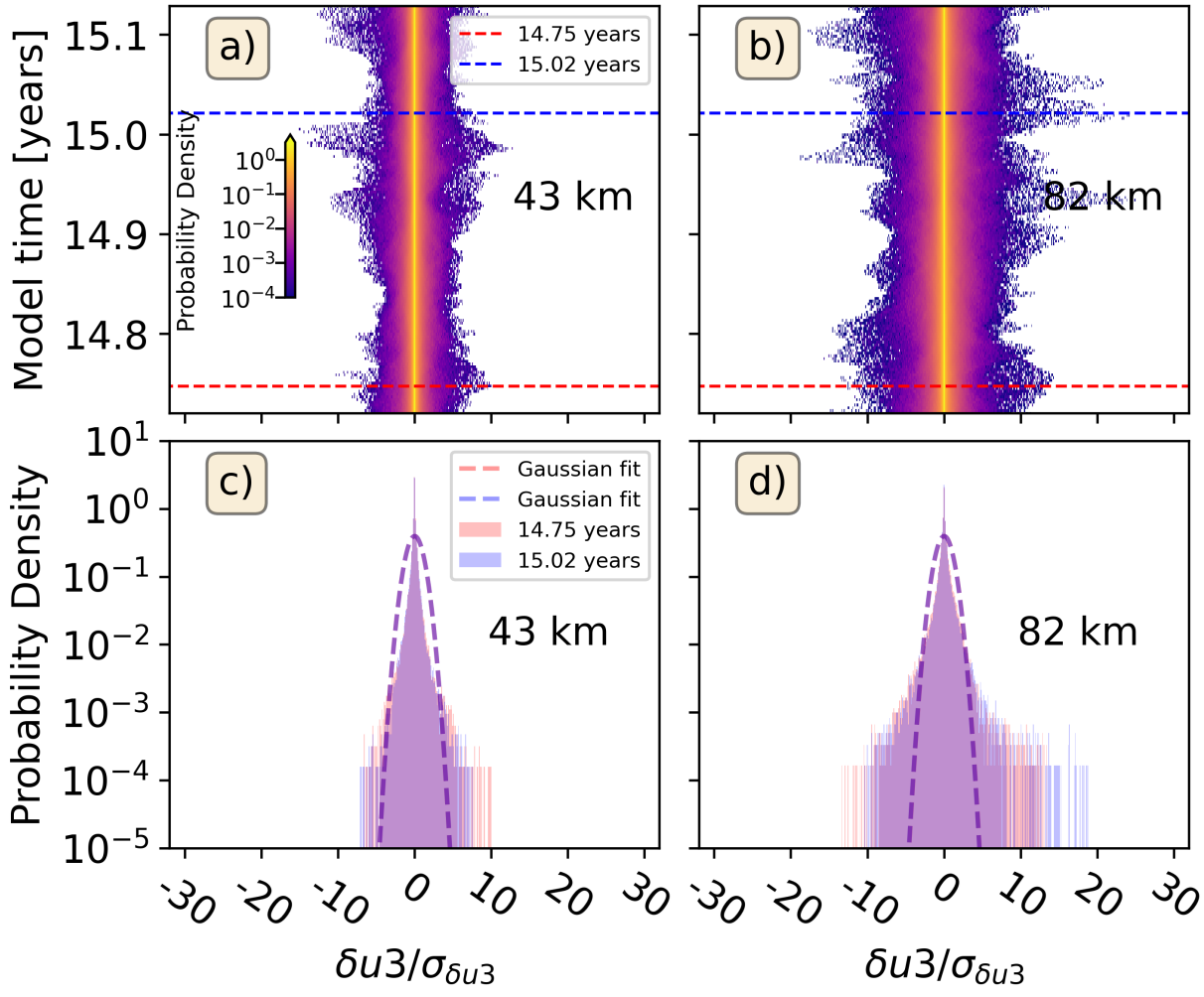

277 FIG. 3. One-year Hovmöller diagram of the probability density ($\log_{10}$ scale) of the daily standard-deviation-
278 normalized third-order structure function samples $\delta u3/\sigma_{\delta u3}$ for the (a) 43- and (b) 82-km r bin. Dashed red and
279 blue lines indicate the 14.75 and 15.02 model year. PDFs of $\delta u3/\sigma_{\delta u3}$ for the (c) 11 km and (d) 105 km r bin.
280 Red and blue bars are the 14.75- and 15.02-year PDFs, respectively. Dashed and solid curves show the Gaussian
281 fit calculated from the mean $\delta u3(\mathbf{s},\mathbf{r},t)$ and standard deviation $\sigma_{\delta u3}$, respectively.

307 and magnitude of the spectral transfers $F_\Pi(k)$, an aspect that the NNLS technique misses. To
308 estimate $F_\Pi(k)$ from (8), horizontal velocity gradients $\nabla\mathbf{u}$ are estimated in spectral space. No
309 detrending or windowing is performed before Fourier transforming as the model is doubly periodic
310 in space. $D3(r)$ from spectral transfer is calculated using (7).

311 $D3(r)$ for the upper-layer (black solid, Fig. 5a) is positive for $r < 100$ km, with a maximum at
312 $r \sim 60$ km, which qualitatively suggests an inverse cascade through its sign. However, at $r > 100$ km,

This manuscript is a non-peer reviewed manuscript submitted to EarthArXiv.
This manuscript is under review for publication in Journal of Atmospheric and Oceanic Technology.
Copyright in this Work may be transferred without further notice.

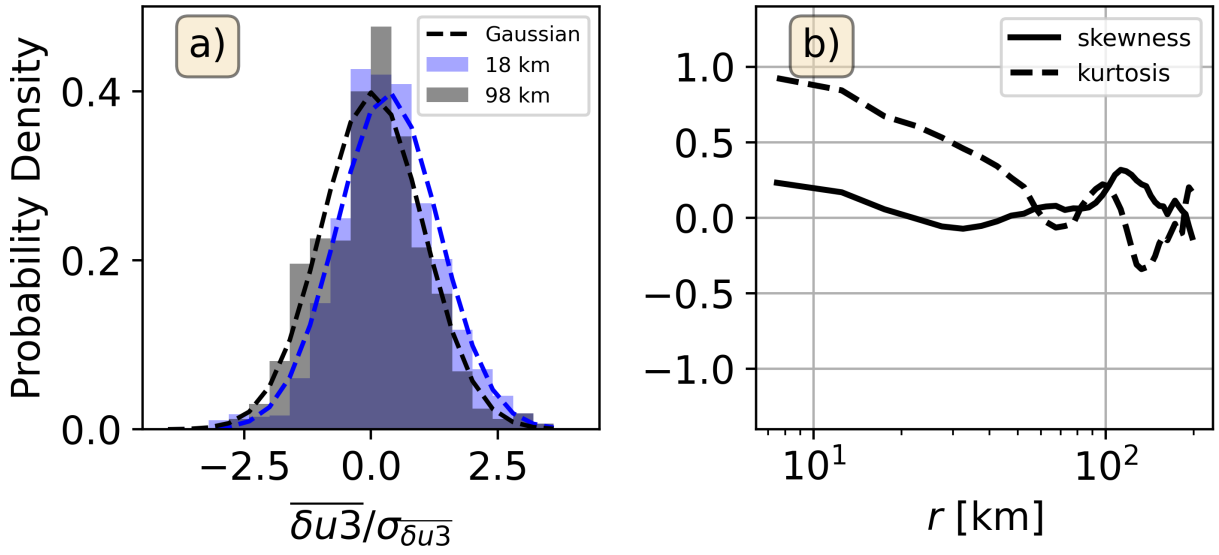

FIG. 4. (a) PDF of standard-deviation-normalized daily averaged third-order structure function samples $\overline{\delta u3}/\sigma_{\overline{\delta u3}}$ for 18 km (gray) and 98 km (blue) bins calculated using 5-year daily snapshots. Dashed lines show the Gaussian fit to the PDF. Solid lines represent the CDF (right y-axis). (b) Skewness (solid) and excess kurtosis (dashed). For a Gaussian distribution, skewness and excess kurtosis are both zero.

$D3_L(r)$ takes on a negative value, even though the spectral transfer $F_\Pi(k)$ exhibits no indication of a forward cascade at these scales (blue line, Fig. 5d). This negative lobe in $D3(r)$ is thus a result of the Bessel function in (7) and stands as a cautionary example of situations when the sign of $D3(r)$ is a misleading indicator of the energy transfer directionality. Thus, it is beneficial to estimate $F(k)$ by inverting (10) rather than relying on the sign of $D3(r)$.

Apart from the assumptions of Gaussianity required for RLS, the structure-function framework described in section 2 also requires that the turbulent flow be homogeneous over the spatial and temporal domain being considered and that the mean flow have no gradients. Since we generated data from a periodic simulation with a prescribed constant background flow, both these assumptions are satisfied by construction (also visually apparent in Fig. 1). However, it should be noted that if we only observed the system over short periods, it would be hard to assess whether the background mean is zero or not, just from the data (see Appendix C). Since the assumptions of the structure-function framework and the RLS approach are satisfied in this context, we proceed to set up the

This manuscript is a non-peer reviewed manuscript submitted to EarthArXiv.
This manuscript is under review for publication in Journal of Atmospheric and Oceanic Technology.
Copyright in this Work may be transferred without further notice.

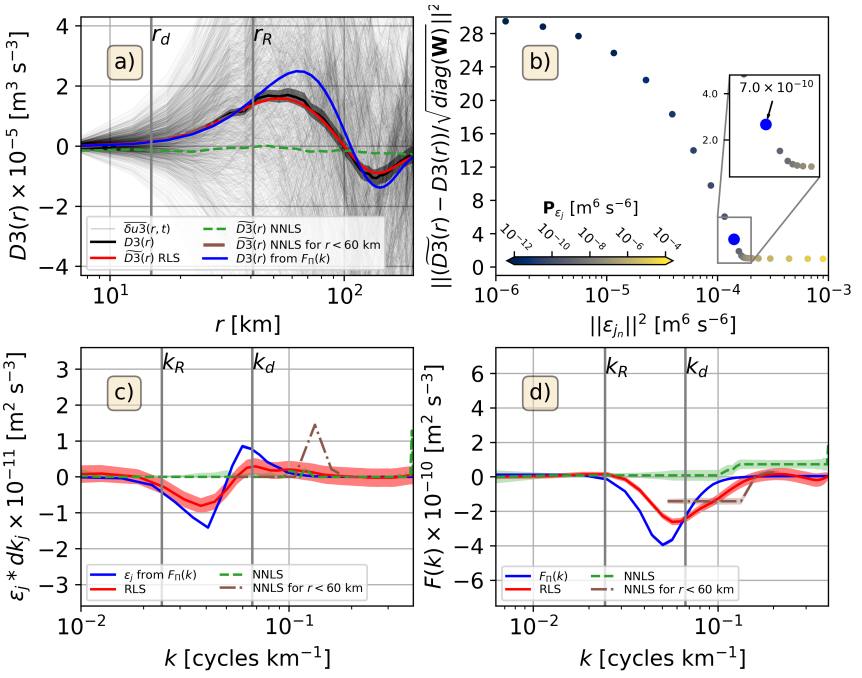

FIG. 5. (a) Third-order structure function $D3(r)$ [m^3 s^{-3}] for the model's upper layer (black solid). Standard errors (prior uncertainty) are shown in shaded gray. Daily $\overline{\delta u 3}(r,t)$ (samples averaged for all positions and orientations) is shown in gray solid lines. Green dashed and red solid curves are the fitted structure function $\widetilde{D3}(r)$ using non-negative least-squares (NNLS; Balwada et al. 2022) and regularized least-squares (RLS; 13), respectively. Brown dash-dotted line is the $\widetilde{D3}(r)$ calculated using NNLS for $r < 60$ km. $D3(r)$ estimated via (7) using the KE transfers calculated using the spectral method $F_\Pi(k)$ (10) is shown in blue solid. Solid vertical line shows the model's Rossby baroclinic radius r_d and Rhine's scale r_R. (b) Trade-off L-curve for different squared uncertainties employed for $\mathbf{P}_{\epsilon_j}$ (color bar). The x-axis shows the L2 norm of the fitted parameters ϵ_j [m^6 s^{-6}]. The L2 norm of the residuals normalized by the uncertainty of $D3(r)$ are shown in the y-axis. Small inset shows where the fitted structure function $\widetilde{D3}(r)$ resembles the calculated $D3(r)$. Optimal value $\mathbf{P}_{\epsilon_j} = 7 \times 10^{-10}$ m^6 s^{-6} used in this study is shown (blue dot). (c) KE injection rates $\epsilon_j * dk$ (divergence of KE transfers) [m^2 s^{-3}]. Positive values indicate divergence of KE transfer. (d) Cross-scale KE transfers $F(k)$ [m^2 s^{-3}]. Positive and negative transfers indicate a forward (downscale) and inverse (upscale) KE cascade. Red solid, green dashed, and brown dashed lines in (c)-(d) are estimated using RLS and NNLS for the full r bins and using $D3(r)$ where $r < 60$ km, respectively. Blue solid line represent $\epsilon_{jC} * dk$ and $F(k)_c$ estimated using the spectral method (14). Red shaded areas in (c)-(d) show the uncertainties in the estimated $\epsilon_j * dk$ and $F(k)$ using RLS as $\sqrt{\text{diag}(\mathbf{C_{xx}})}$ (14) and $\sqrt{\text{diag}(\mathbf{F_{xx}})}$ (15), respectively. The standard error of the spectral-based estimates is shown in blue shaded. Brown and green shaded in (c)-(d) are the NNLS-based standard errors, respectively. Vertical solid lines in (c)-(d) show the model's Rhines wavenumber k_R and Rossby wavenumber k_d.

This manuscript is a non-peer reviewed manuscript submitted to EarthArXiv.
This manuscript is under review for publication in Journal of Atmospheric and Oceanic Technology.
Copyright in this Work may be transferred without further notice.

RLS problem. This involves constructing the matrices for the prior data uncertainty $\mathbf{W}$ and the prior uncertainty of the fitted parameters $\mathbf{P}$.

The prior uncertainty of $D3(r)$ is estimated by calculating the standard error, i.e., the standard deviation of the daily samples of the five-year mean ($\overline{\delta u 3}(r,t)$; gray solid, Fig. 5a) divided by the square root of the degrees of freedom $\sqrt{N(r)}$ (see Appendix B). Here, the degrees of freedom are not simply the number of days since $\overline{\delta u 3}(r,t)$ is not an independent sample each day. To estimate $N(r)$, we first calculate the scale-dependent decorrelation time scale $T_{scale}(r)$ following Balwada et al. (2022) by using the second-order structure function as $D2(r)/r$ (black solid, Fig. C1c). Subsequently, the scale-dependent degrees of freedom $N(r)$ are computed using $T_{scale}(r)$ and the total number of days (red solid, Fig. C1c). We use the square of the standard errors in $D3(r)$ (shaded gray, Fig. 5a) as the diagonal of $\mathbf{W}$; the off-diagonal elements are set to zero.

There is no physical guidance on how to set prior uncertainty for the parameters to be estimated, so we construct $\mathbf{P}$ with the help of a heuristic approach called the "L-curve" method. The prior uncertainty is chosen to maximize the fit to the data ($D3(r)$) while keeping the size of the fitted parameters ϵ_j small. This "sweet-spot" is determined by estimating a trade-off between the L2 norm of the estimated ϵ_j and the L2 norm of the model–data misfit normalized by $\sigma_{\overline{\delta u 3}}/\sqrt{N}$ (Fig. 5b). This heuristic approach is a way to avoid overfitting.

Choosing a larger prior uncertainty for ϵ_j reduces the misfit but increases the size of ϵ_j (overfits), thus the posterior uncertainty. Conversely, the data–model misfit increases as the prior uncertainty decreases (over-smoothed solution). Using this method, the $\mathbf{P}$ diagonal's first element is selected as 10^{-7} m^4 s^{-6} corresponding to the squared prior uncertainty in ϵ_u, whereas 7×10^{-10} m^2 s^{-6} was chosen as the prior uncertainty in ϵ_j for the rest of the diagonal elements.

We perform a fit to $D3(r)$ to test our RLS approach. The corresponding RLS-based estimates of the spectral transfers $F(k)$ and energy injection rates ϵ_j, and the fit to five-year structure function $\widetilde{D3}(r)$ are shown as red solid lines in Fig. 5. The RLS-based structure function $\widetilde{D3}(r)$ calculated by multiplying the model matrix $\mathbf{H}$ with the fitted parameters $\widetilde{\mathbf{x}}$ (red solid, Fig. 5a), approaches $D3(r)$ well and is within the uncertainty bounds (gray shaded, Fig. 5a). The RLS $F(k)$ (red solid, Fig. 5c) indicates the presence of an inverse cascade similar to the spectral transfer $F_\Pi(k)$ (blue solid, Fig. 5c), and the estimated energy injection rates (ϵ_j) match both the positive and negative energy injections (blue solid, Fig. 5d).

This manuscript is a non-peer reviewed manuscript submitted to EarthArXiv.
This manuscript is under review for publication in Journal of Atmospheric and Oceanic Technology.
Copyright in this Work may be transferred without further notice.

3) Comparing RLS to other estimation approaches

We compare the RLS-based estimates against those that may be obtained using NNLS, which was used by Balwada et al. (2022). To estimate the NNLS-based five-year mean $\widetilde{D3}(r)$, ϵ_u, ϵ_j, and $F(k)$, we first estimated the fitted structure function $\widetilde{D3}(r)$ by ensemble averaging $\overline{\delta u 3}(r,t)$ and inverted it using NNLS. Subsequently, we inverted the daily $\overline{\delta u 3}(r,t)$ time series to generate daily estimates used to calculate standard errors. The standard errors were calculated by estimating the standard deviation divided by $\sqrt{N}$, where N is the degrees of freedom at the largest r; this definition of N sets an upper bound for the standard error. As expected, the NNLS application for all r is unable to fit $D3(r)$. Consequently, energy injection rate estimates and spectral transfer are non-physical (green dashed, Fig. 5a,c,d). Therefore, NNLS is ill-suited for estimating convergence of $F(k)$ (i.e., $\epsilon_j \cdot dk_j < 0$).

From (7), we can expect that $F(k)$ behaves as an increasing function of k given that $D3(r)$ increases with r for $r < 60$ km (black solid, Fig. 5b). This assumption is corroborated by the shape of $F_\Pi(k)$, which is an increasing function for $k > 1/60$ cycles km^{-1}. Therefore, we hypothesize that NNLS could potentially capture the size and shape of the ϵ_j and $F(k)$ values for $k > 1/60$ cycles km^{-1} (red and blue solid, Fig. 5c,d). A partial fit may help to recover the shape of $F(k)$ over a partial range of scales. The partial fit and estimates and their standard errors are calculated similarly to the full r range.

The NNLS-based structure function $\widetilde{D3}(r)$ over the partial range matches $D3(r)$ well by eye (brown dashed, Fig. 5a). Unlike the NNLS fit over the full range, the partial $F(k)$ shows the presence of an inverse cascade (brown dashed, Fig. 5d). However, the estimated energy injection rates take on non-zero values at the wrong scale and are a factor of two to five larger than the spectral injection rates (brown dashed, Fig. 5c). The inclusion of the $\mathbf{P}$ matrix in the RLS constrains the size of the fitted parameters, an aspect not included in the NNLS.

In this section, we showed that RLS can estimate the KE transfers – spectral transfers and the energy injection rates – without assuming a prior shape of $F(k)$ or sign of ϵ_j. The RLS method is superior to the NNLS as it constrains the size of the fitted parameters. Also, this approach provides posterior uncertainties for ϵ_u, ϵ_j and propagates the error to estimate uncertainty in $F(k)$. Having established trust in the RLS fits and the $D3(r)$ framework, we proceed in the next subsection to

This manuscript is a non-peer reviewed manuscript submitted to EarthArXiv.
This manuscript is under review for publication in Journal of Atmospheric and Oceanic Technology.
Copyright in this Work may be transferred without further notice.

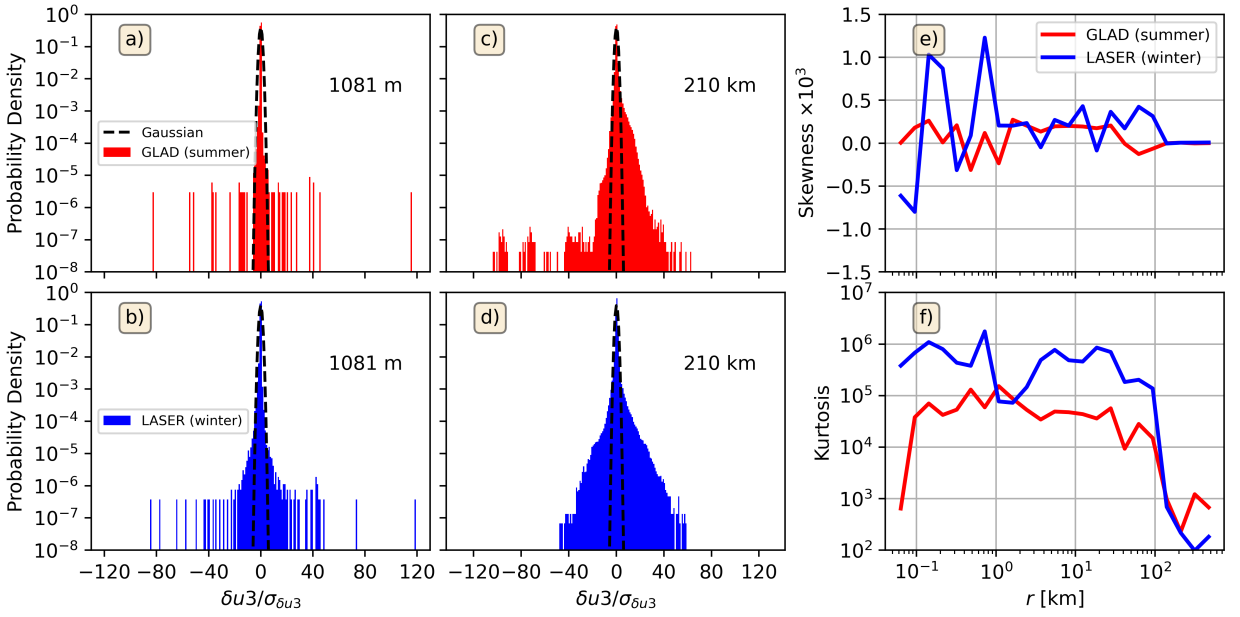

FIG. 6. PDF for the (a),(c) GLAD (summer; red) and (b),(d) LASER (winter; blue) standard-deviation-normalized third-order structure function $\delta u3/\sigma_{\delta u3}$ for the (a)-(b) 1 km and (c)-(d) 210 km bins. The y-axis is in log scale. Dashed lines correspond to the Gaussian fits. (e) Skewness and (f) excess kurtosis of $\delta u3(\mathbf{s},\mathbf{r},t)$ for the GLAD (red) and LASER (blue) experiments.

show the application of the improved methodology to sparse drifter data and compare the ϵ_j and $F(k)$ estimated using RLS with those estimated by Balwada et al. (2022) using NNLS.

b. Application for sparse drifter data

1) PAIR-SAMPLE DISTRIBUTION OF $\delta u3$ AND UNCERTAINTY OF $D3(r)$

For the drifter data, as for the QG model, we start by considering the distribution from the pair samples of $\delta u3(\mathbf{s},\mathbf{r},t)$ for each season, which are ensemble-averaged to estimate the third-order structure function $D3(r)$. Unlike the dense gridded sampling from the QG simulations, the drifters only sample $\delta u3(\mathbf{s},\mathbf{r},t)$ at sparse spatial locations ($\mathbf{s}$) and orientations ($\mathbf{r}$). Akin to the QG model, the distributions from the drifters are highly non-Gaussian, with long tails and occasional outliers as large as $115\sigma_{\delta u3}$ (Fig. 6a,b). Large skewness and kurtosis for all r bins confirm that the distribution of $\delta u3(\mathbf{s},\mathbf{r},t)$ is non-Gaussian (Fig. 6e,f), which does not fulfill the RLS requirement that errors have Gaussian distributions.

This manuscript is a non-peer reviewed manuscript submitted to EarthArXiv.
This manuscript is under review for publication in Journal of Atmospheric and Oceanic Technology.
Copyright in this Work may be transferred without further notice.

For computing the corresponding uncertainty estimate, we use a bootstrapping approach. Standard bootstrapping assumes that all data samples (pair samples of $\delta u3$ in this case) are independent, which yields unrealistically small standard errors (one-to-two orders of magnitude smaller than the mean $D3(r)$), hence small posterior ϵ_j, ϵ_u and $F(k)$ uncertainties (not shown). However, we know that many pair samples are correlated due to proximity in space or time, and this needs to be accounted for. To overcome this difficulty, we use moving-block bootstrapping, an approach to estimate proper uncertainty when the contributing samples are correlated (Kunsch 1989).

For moving-block bootstrapping, we construct a pseudo-time series of $\delta u3(r,t)$ for each r bin from several concatenated time series of different pairs of drifters. The concatenated records inherently have some autocorrelation because of the spatio-temporal proximity between pairs. Then we divided the concatenated $\delta u3(r,t)$ data for each r bin into overlapping blocks of data of size $L(r)/N(r)$, where $L(r)$ is the length of the concatenated data per r bin and $N(r)$ is the number degrees of freedom. Here, $N(r)$ is roughly estimated by dividing the total duration of each drifter experiment by the decorrelation timescale at each r, which was calculated with the help of $D2(r)$ (see Appendix B; Fig. B2). Next, we sample b blocks with replacement at each r and concatenate them to construct a pseudo-time series of $\delta u3(r,t)$ of length $L(r)$. The mean of this pair-sample set gives a bootstrap estimate of $D3(r)$ ($D3_b(r)$). We repeat this step 2000 times to ensure that the bootstrap estimates $D3(r)_b$ are Gaussian-distributed by the central limit theorem (Stroock 2010). This moving-block bootstrapping contrasts with that used by Balwada et al. (2022), where the concatenated block of size $L(r)$ was divided into $N(r)$ blocks.

PDFs of the $D3(r)_b$ for selected r bins show Gaussian distributions for both experiments (Fig. 7a,b). The near-zero skewness and excess kurtosis for most of the r bins confirm that the bootstrapped quantities have Gaussian distributions (Fig. 7c,d). The smallest r bins for the LASER experiment (blue solid) show large negative skewness and excess kurtosis (Fig. 7c,d) due to the large outliers in the concatenated data. However, the RLS results are insensitive to the inclusion or removal of these two bins. The prior uncertainty in $D3(r)$ was estimated by computing the standard deviation of these bootstrapped $D3_b(r)$ distributions.

This manuscript is a non-peer reviewed manuscript submitted to EarthArXiv.
This manuscript is under review for publication in Journal of Atmospheric and Oceanic Technology.
Copyright in this Work may be transferred without further notice.

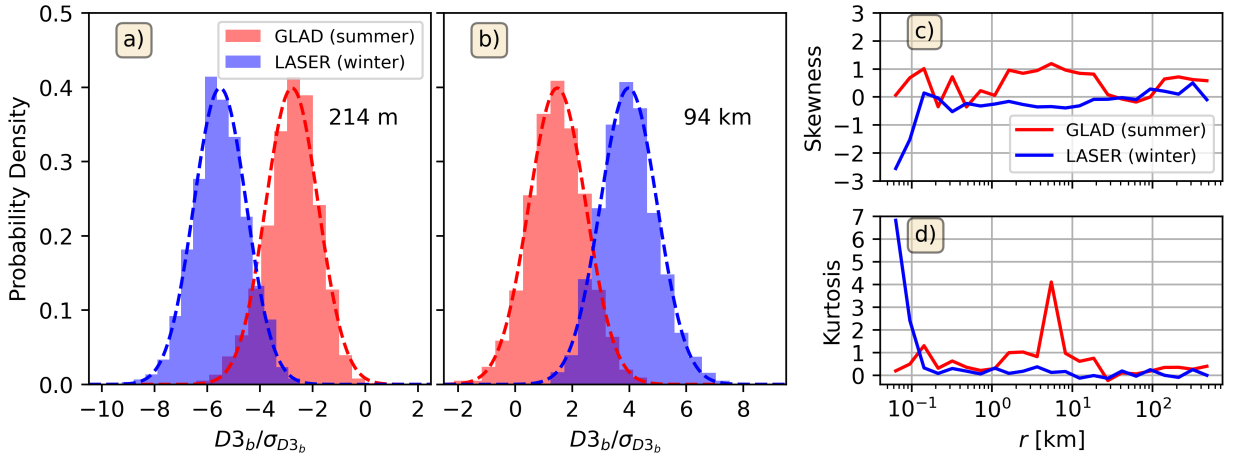

FIG. 7. (a)-(b) PDFs of bootstrapped means $D3_b/\sigma_{D3_b}$ generated using moving-block bootstrapping for GLAD (red) and LASER (blue) experiments, respectively. Dashed lines show the Gaussian distribution. Only the (a) 214 m and (b) 94 km bins are shown. (c) Skewness and (d) excess kurtosis estimated for the bootstrapped means.

2) Application of improved methodology to sparse observations

Next, we apply the RLS approach to deduce the seasonality of the KE transfers and injection rates by inverting (10) with the observed $D3(r)$ from the summertime GLAD and wintertime LASER experiments (Fig. 8a,b). Both calculated $D3(r)$ qualitatively suggest the presence of bi-directional energy transfers as they transition from negative to positive values as r increases. In contrast to winter (Fig. 8b), the summertime $D3(r)$ could indicate that $F(k)$ does not purely increase with k since $D3(r)$ decreases slightly between 10 km $\leq r \leq$ 60 km (Fig. 8a). We presume the decrease over this range of scales indicates convergence of $F(k)$ (i.e., $\epsilon_j < 0$). However, the first-order structure function $D1(r)$ for both seasons shows that the condition of homogeneity is not satisfied for all r with the limited sampling (i.e., $D1(r) \neq 0$; see Appendix C, Fig. C2a). We proceed with caution in interpreting our results.

To set up the RLS method, the moving-bootstrapped estimates of errors shown in Fig. 8a,b (shaded areas) are used to construct the diagonal of $\mathbf{W}$ as the square of the prior uncertainty. Similar to the QG model, we set the prior uncertainty of ϵ_j^2 (diagonal of $\mathbf{P}$) as 4×10^{-7} m^6 s^{-6} after using the "L-curve" method (not shown). We also compared our RLS estimates with estimates derived using NNLS (Balwada et al. 2022). To estimate the uncertainty in the NNLS-based ϵ_j and $F(k)$ for each season per r bin, we invert the 2000 bootstrap means $D3_b(r)$ to estimate 2000

This manuscript is a non-peer reviewed manuscript submitted to EarthArXiv.
This manuscript is under review for publication in Journal of Atmospheric and Oceanic Technology.
Copyright in this Work may be transferred without further notice.

bootstrapped ϵ_j (10) and $F(k)$ (9). The standard deviation of these estimates provides a measure of the prior uncertainty.

The RLS-based $D3(r)$ matches the observed $D3(r)$ better than the NNLS fit for both seasons (Fig. 8a,b). The NNLS fit fails (thin orange solid) to capture the second minimum in the GLAD $D3(r)$ located at $r \sim 60$ km (thick red solid, Fig. 8a). The RLS-based estimates of ϵ_j are smoother and smaller in amplitude (with smaller posterior uncertainties) than the NNLS estimates (Fig. 8c,d). Moreover, the NNLS fit fails to estimate any negative energy injection rates by design, whereas the RLS-based ϵ_j values suggest the presence of such negative transfers, as seen in the summer (red solid) at intermediate scales of $k \sim 0.07$ cycles km^{-1} and LASER (blue solid) at large scales of $k \sim 9 \times 10^{-3}$ cycles km^{-1} (Fig. 8c,d, respectively).

The KE transfers $F(k)$ estimated using RLS (thin red and blue solid, Fig. 8e,f, respectively) follow a similar shape and amplitude as those estimated using NNLS (thin orange and turquoise solid, Fig. 8e,f, respectively): a bi-directional KE transfer where an inverse cascade dominates at mesoscales and forward cascade is present at submesoscales. The transition scale from inverse to forward cascade shows a seasonal modulation. While the RLS- and NNLS-based $F(k)$ estimates are not statistically distinguishable for each season (except during summer at $k \sim 0.05$ cycles km^{-1}), on average, the RLS fitting yields smaller uncertainties than the NNLS.

6. Summary and Discussion

An improved methodology to estimate cross-scale KE transfers and injection rates (divergence of the cross-scale KE transfers) using third-order structure functions $D3(r)$ has been presented in this study. The method employs a recently developed theory by Xie and Bühler (2019) used by Balwada et al. (2022) to relate $D3(r)$ to KE transfers $F(k)$ under assumptions of homogeneity and isotropy. The improved methodology employs regularized least-squares, allowing us to estimate posterior uncertainty in the KE transfers and its divergence by including the prior uncertainty in the estimated third-order structure function $D3(r)$ and expected fitted parameters (i.e., KE injection rates ϵ_u, ϵ_j). The regularized least-squares method constrains the size of the fitted parameters with the inclusion of the prior uncertainty and reduces overfitting, yielding physical KE injection rates. In contrast, ordinary and non-negative least squares may produce unconstrained non-physical rates.

This manuscript is a non-peer reviewed manuscript submitted to EarthArXiv.
This manuscript is under review for publication in Journal of Atmospheric and Oceanic Technology.
Copyright in this Work may be transferred without further notice.

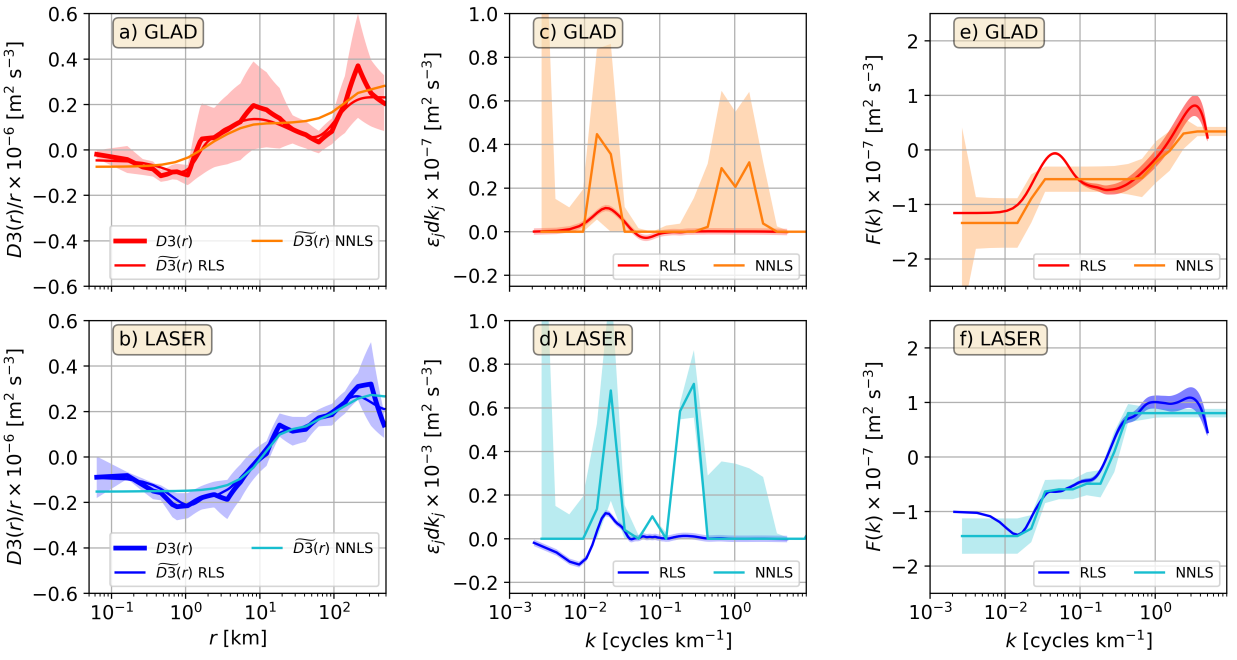

484 FIG. 8. GLAD (red; top row) and LASER (blue; bottom row) (a)-(b) normalized third-order structure function
485 $D3(r)/r$, (c)-(d) KE injection rates $\epsilon_j dk_j$ [m^2 s^{-3}] and (e)-(f) KE transfers $F(k)$ [m^2 s^{-3}]. Thin red and
486 blue and orange and turquoise solid lines show variables estimated using RLS and NNLS fitting, respectively.
487 Shaded areas in (a)-(b) are the prior uncertainties of $D3(r)$. Light and dark-shaded areas are the NNLS-based
488 bootstrapped standard error and the RLS posterior uncertainties, respectively. Positive and negative ϵ_j in (c)-(d)
489 indicate divergence and convergence of KE transfer, respectively. Forward (downscale) and inverse (upscale)
490 cascade are denoted by positive and negative $F(k)$ in (e)-(f).

502 The improved methodology has been applied first to a two-layer QG model to test whether
503 the regularized least-squares method reproduces the inverse cascade expected for QG turbulence
504 (Charney 1971). The regularized least-squares approach requires Gaussian-distributed errors in $\mathbf{x}$
505 (fitted parameters) and $\mathbf{e}$ (data). Since the samples of the third-order structure function $\delta u3(\mathbf{s},\mathbf{r},t)$
506 are non-Gaussian distributed (Fig. 3), we averaged $\delta u3(\mathbf{s},\mathbf{r},t)$ over all positions and orientations at
507 each time to produce a time series of spatially-averaged third-order structure functions $\overline{\delta u3}(r,t)$.
508 By the central limit theorem, the averaging produces Gaussian distributed samples (Fig. 4; Stroock
509 2010). We then estimate the standard error in $D3(r)$ using $\overline{\delta u3}(r,t)$ and employ it in the regularized
510 least-squares fitting as the prior uncertainty in $D3(r)$.

This manuscript is a non-peer reviewed manuscript submitted to EarthArXiv.
This manuscript is under review for publication in Journal of Atmospheric and Oceanic Technology.
Copyright in this Work may be transferred without further notice.

Our findings show that the improved methodology captures the shape of $D3(r)$, the convergence of KE transfers $\epsilon_j < 0$, and the inverse cascade $F(k) < 0$ that peaks at the prescribed baroclinic Rossby wavenumber k_d as shown by the spectral method (Fig. 5). As expected, we show that the non-negative least squares approach (Balwada et al. 2022), by definition, is not well-adapted to resolve convergence of KE transfer $\epsilon_j < 0$ (Fig. 5c) or to identify times when KE transfer is not an increasing function of k (Fig. 5d). When $D3(r)$ is selected for $r < 60$ km, the non-negative least-squares fitting resolves the shape of the spectral transfers $F_\Pi(k)$, i.e., the inverse cascade decreases to zero with k (brown dashed line, Fig. 5d). Nonetheless, ϵ_j values are larger than those estimated using regularized least-squares and spectral method for $D3(r)$ with all r bins (Fig. 5c). The sizes of the non-negative least-squares injection rates are unconstrained, yielding larger non-physical injection rates and step-like $F(k)$. The regularized least-squares method constrains the size of the fitted parameters (with some bias), resulting in realistic injection rates and transfers with smoother shapes than those estimated using non-negative least squares.

After testing the improved methodology on the QG model, we then applied the regularized least-squares method to the summertime GLAD and wintertime LASER experiment drifter datasets (Balwada et al. 2022) to analyze the bi-directional KE transfers across seasons. Both GLAD and LASER $\delta u3(\mathbf{s}, \mathbf{r}, t)$ show long-tailed PDFs (excess kurtosis $> O(10^2)$), especially at submesoscales ($r < O(10)$ km) where a few yet large ($\delta u3/\sigma_{\delta u3} > 10$) events are shown (Fig. 6). The non-Gaussian distribution of $\delta u3(\mathbf{s}, \mathbf{r}, t)$ across all scales breaks the assumption of Gaussian-distributed errors required by the regularized least squares. As an alternative, moving-block bootstrapping was used to improve the calculation of the uncertainties in $D3(r)$, generating Gaussian-distributed mean $D3(r)$ per r bin (Fig. 7) and using the bootstrapped standard deviation as the prior uncertainty $\mathbf{W}$. The regularized-least-squares-based ϵ_j and $F(k)$ agree with results found by Balwada et al. (2022) using non-negative least-squares (Fig. 8). Both methods yield a bi-directional cascade where $F(k)$ transitions from an inverse cascade at mesoscale to a forward cascade for submesoscales. The transition from inverse to forward cascade ($F(k) = 0$) exhibits a seasonal modulation, with the transition shifting from $k \sim 1$ cycles km^{-1} during summer to $k \sim 0.02$ cycles km^{-1} in winter. Balwada et al. (2022) attributed the seasonal modulation of the transition of the KE transfers to the KE injected ($\epsilon_j > 0$) at scales near the scale of the most unstable wave within the mixed layer in the form of submesoscale instabilities. The instabilities are the largest during winter as a consequence

This manuscript is a non-peer reviewed manuscript submitted to EarthArXiv.
This manuscript is under review for publication in Journal of Atmospheric and Oceanic Technology.
Copyright in this Work may be transferred without further notice.

of the deepening of the mixed layer, which stores more potential energy to be released by baroclinic instabilities with larger scales (Boccaletti et al. 2007; Fox-Kemper et al. 2008).

In contrast to the non-negative least-squares fitting, regularized least squares shows a significant convergence of KE transfer ($\epsilon_j < 0$) during the summer ($k \sim 0.07$ cycles km^{-1}; red solid in Fig. 8c) and winter ($k \sim 9 \times 10^{-3}$ cycles km^{-1}; blue solid in Fig. 8d) seasons. The convergence found during the summer significantly enhances the inverse cascade between 0.05 cycles km^{-1} and 0.30 cycles km^{-1}, potentially shifting the transition from negative to positive $F(k)$ to 1 cycles km^{-1} (red solid, Fig. 8e). Undoubtedly, the effect of the convergence of KE transfer in shifting the zero $F(k)$ crossing to a smaller scale is forfeited by the non-negative least-squares due to their incapacity to detect convergences. The convergence could stem from wind-driven damping, dissipation of KE, transfer of KE to potential energy, or vertical transfer of KE below the surface and the mixed-layer base. For future work, simultaneous observations of temperature, salinity, and ocean velocity that resolve submesoscale processes could be used in conjunction with third-order structure functions for stratified turbulence and the improved methodology presented in this study to analyze the cross-scales transfers of available potential energy (Deusebio et al. 2014).

Adequately estimating the prior uncertainty in $D3(r)$ is paramount for estimating the KE cascade more accurately as it has a significant impact on the posterior uncertainty in ϵ_j and $F(k)$. Averaging over all orientations and positions in the QG model and moving-block bootstrapping for the drifter datasets deliver uncertainties that might be too low as both methods average all events, masking the intermittent strong events found in the heavily tailed distributions that shape the amplitude and sign of the mean $D3(r)$ (Figs. 2,6). Moreover, the uncertainty in the averaged samples and bootstrapped means is not incorporated into the prior uncertainty of $D3(r)$. For instance, the resulting $F(k)$ in the drifter datasets could misleadingly indicate the presence of a forward cascade that operates due to repeated events of similar amplitude. An alternative approach for estimating prior uncertainties in $D3(r)$ inherent in limited sampling settings is parametric bootstrapping, where the data are adjusted to a PDF such as normal-inverse Gaussian distribution (DeMarco and Basu 2017; Barndorff-Nielsen et al. 2004) that best fits the data PDF (potentially using maximum likelihood estimation), and then bootstrapping is carried out using the adjusted data. This method has proved useful, yielding uncertainties in high-order structure functions with relatively less bias (DeMarco and Basu 2017). Additionally, observation-based uncertainties in $D3(r)$ should include

This manuscript is a non-peer reviewed manuscript submitted to EarthArXiv.
This manuscript is under review for publication in Journal of Atmospheric and Oceanic Technology.
Copyright in this Work may be transferred without further notice.

a full budget accounting for sampling biases and instrument errors (e.g., positioning and instrument error).

As demonstrated in this study, the improved methodology, in combination with the $D3(r)$ framework, can be used for both gridded and sparse ungridded data, whereas the spectral and coarse-graining methods require gridded data to estimate velocity gradients (Srinivasan et al. 2023; Ajayi et al. 2021). Advective structure functions (Pearson et al. 2021) are useful for estimating KE and enstrophy transfers in anisotropic flows. Still, they require estimating velocity gradients and are unsuited for detecting forcing scales. Also, isotropy is not satisfied in areas such as western boundary currents, the frontal jets of the Antarctic Circumpolar Current, and along-shelf currents. The homogeneity condition in the Karman–Howarth–Monin equation (Frisch 1995) may also not be satisfied, potentially obscuring the eddy–eddy interactions encapsulated in $D3(r)$. The drifters' $D1(r) \neq 0$ (Fig. C2a) suggests that the homogeneity condition is not satisfied as drifters potentially sample flows with large divergence or vorticity in the background flow (Pearson et al. 2020), which could impact the interpretation of the KE transfers. While the QG model $D1(r) \sim 0$ indicates a certain level of homogeneity, the temporal variability of $\overline{\delta u 1}(r,t)$ (Fig. C1a) shows that assessing homogeneity is challenging when flows are sampled over short periods. Sampling with adequate spatiotemporal resolution enables a more accurate estimation of the mean flow, which allows us to remove the mean flow from the velocity field. This, in turn, helps us better estimate velocity fluctuations and structure functions, as well as meet the homogeneity requirement.

As shown by Srinivasan et al. (2023), the forward cascade in the ocean is significantly driven by divergent submesoscale frontogenesis, which is highly anisotropic. Thus, we would like to know whether the improved methodology and structure-function framework could capture the forward cascade if sampling many anisotropic events with different shapes and orientations. Testing our method using submesoscale resolving ocean model outputs (with the possibility of submesoscale-resolving observations to be assimilated) to estimate the energy cascade and to compare it to that calculated using the coarse-graining method could shed light on the robustness of this study's improved methodology.

Most ocean observations, such as drifters, shipboard acoustic Doppler current profiler transects, and autonomous platforms, provide ungridded ocean velocity data that can be used to quantify and study the KE cascade by exploiting the improved methodology presented in this study. A better

This manuscript is a non-peer reviewed manuscript submitted to EarthArXiv.
This manuscript is under review for publication in Journal of Atmospheric and Oceanic Technology.
Copyright in this Work may be transferred without further notice.

understanding of the KE cascade could improve existing ocean parameterizations and create new parameterizations for global climate models.

Data availability statement. The code for the PyQG model is made available in `https://doi.org/10.5281/zenodo.6380711`, and documentation is available in `https://pyqg.readthedocs.io/en/latest/`. The GLAD and LASER experiment drifter data can be accessed in `https://data.gulfresearchinitiative.org/`. MATLAB code for processing the drifter data and calculating the structure functions is found in `https://github.com/dhruvbalwada/SF3_to_KEflux`. Python code is available for estimating structure functions and energy transfers with regularized least-squares in `https://github.com/manuelogtzv/SF3_RLS`. Arch 6.3.1 (python library) used to estimate the moving-block bootstrapping (Sheppard et al. 2024) is available in `https://arch.readthedocs.io/en/latest/index.html` and `https://zenodo.org/records/10981635`.

Acknowledgments. M. O. G. V., S. T. G., and M. M. have been supported by the NASA Surface Water and Ocean Topography Science Team (NASA 80NSSC20K1136, 80NSSC24K1657), the NASA Ocean Vector Winds Science Team (80NSSC19K0059), and the NASA Ocean Surface Topography Science Team (80NSSC21K1822). D. B. acknowledges support from NSF grant OCE-2242110. B. C. acknowledges support from ONR grant N000142112726.

APPENDIX A

Equations for two-layer QG model

In this appendix, we provide details about the equations solved in the two-layer QG model (PyQG; Abernathey et al. 2022). The model uses QG potential vorticity in the upper q_1 and lower q_2 layers as prognostic variables:

$$q_m = \nabla^2 \Psi_m + (-1)^m F_m (\Psi_1 - \Psi_2), \quad m = 1, 2 \tag{A1}$$

where Ψ_m is geostrophic streamfunction in layer m with thickness H_m, $F_1 = k_d^2/(1+\alpha)$, and $F_2 = \alpha F_1$, where

$$k_d^2 = \frac{f_o^2}{g'} \frac{H_1 + H_2}{H_1 H_2} \tag{A2}$$

This manuscript is a non-peer reviewed manuscript submitted to EarthArXiv.
This manuscript is under review for publication in Journal of Atmospheric and Oceanic Technology.
Copyright in this Work may be transferred without further notice.

is the baroclinic Rossby deformation wavenumber, $\alpha = H_1/H_2$ is the layer thickness ratio, f_o is the local Coriolis frequency, and g' is reduced gravity. Ψ_m is diagnosed from q_m by integrating the Laplacian using periodic boundary conditions. The horizontal velocity components are calculated using the Ψ_m:

$$u_m = -\partial_y \Psi_m, \quad v_m = \partial_x \Psi_m. \tag{A3}$$

The model solves the evolution of the QG potential vorticity field in spectral space $\Psi_m = \sum \widehat{\Psi}_m e^{ikx}$:

$$\partial_t \widehat{q_m} = -\widehat{\mathrm{J}}(\Psi_m, q_m) - \mathrm{i}k_x \beta \widehat{\Psi}_m - \mathrm{i}k_x U_m \widehat{\Psi}_m + \delta_{m,2} r_{ek} k^2 \hat{\Psi}_2 + \widehat{\mathrm{SSD}}, \tag{A4}$$

where U_m is the background flow, ∂_t is the Eulerian time derivative, and $\mathrm{J}(\Psi_m, q_m) = \partial_x \Psi_m \partial_y q_m - \partial_y \Psi_m \partial_x q_m$ is the Jacobian in physical space. The change in the Coriolis frequency with latitude y is defined as $f_o + \beta y$ with a slope β. $\delta_{m,2}$ is the Kronecker delta function, and r_{ek} is the bottom drag coefficient applied only to the second layer to dissipate large-scale energy. The small-scale dissipation, SSD, absorbs enstrophy that cascades toward small scales and is set as an exponential filter:

$$E_f(k^*) = \begin{cases} 1 & k^* < k_c \\ e^{-23.6(k^* - k_c)^4}, & k^* \geq k_c \end{cases}, \tag{A5}$$

where $k^* = \sqrt{(k_x * \Delta x)^2 + (k_y * \Delta y)^2}$ is the non-dimensional wavenumber, $\Delta x = \Delta y = 3.9$ km are the spatial grid spacing, and $k_c = 0.65\pi$ is the non-dimensional cut-off wavenumber. The filter reduces aliasing errors and provides stable simulations with necessary numerical dissipation (Ross et al. 2023), and attenuates the highest third of wavenumbers of all terms in the right-side of (A3). More details about the model's solution are found in Abernathey et al. (2022).

APPENDIX B

Second-order structure function and degrees of freedom

Here we show the second-order structure function $D2(r)$ and the degrees of freedom estimated from the QG model u, v outputs, and the drifter data. We follow Balwada et al. (2022) and employ

This manuscript is a non-peer reviewed manuscript submitted to EarthArXiv.
This manuscript is under review for publication in Journal of Atmospheric and Oceanic Technology.
Copyright in this Work may be transferred without further notice.

$D2(r)$ to estimate the degrees of freedom $N(r)$ as

$$T_{scale}(r) = r/\sqrt{D2(r)}, \tag{B1}$$

$$N(r) = T_{tot}/T_{scale}(r), \tag{B2}$$

where T_{tot} is the duration of the model's time series used for the analysis (5 years) and 90 and 60 days for the summer GLAD and wintertime LASER drifter data sets, respectively.

QG model

To carry out the improved methodology in the QG model output, we first need to evaluate $D2(r)$ in the context of the isotropic KE spectrum $E(k)$ using 5 as $D2(r)$ is employed to calculate the degrees of freedom $N(r)$. In this subsection, we estimate $E(k)$ using the last five years of the daily averaged horizontal velocity fields (u, v; offline diagnostic) to analyze the expected dynamics in the QG model. In estimating the KE spectrum, no detrending or windowing is needed or used as the model is double periodic in space. The wavenumber spectrum is close to a k^{-3} power law, potentially indicating QG turbulence (Fig. B1a, Charney 1971). A steep drop in spectral density at 0.10 cycles km^{-1} corresponds to the spectral filter's wavenumber cutoff. Our results are unchanged when $E(k)$ is calculated using hourly snapshots for the model output's last year (green solid) except for the smallest k.

Next, we transform $E(k)$ to second-order structure function $D2(r)$ (5) and compare it to $D2(r)$ calculated directly from the model's velocity output (Fig. B1b). The theoretical $D2$ (blue solid) lies on top of the estimated $D2$ (black solid) and within the spatially-averaged estimates $\overline{\delta u 2}(r,t)$ (red solid) (Fig. B1b) following a r^2 power law for $r \leq 20$ km. The theoretical and estimated $D2(r)$ show a shallower r relationship for 30 km$< r <$ 70 km. We used $D2(r)$ to estimate $T_{scale}(r)$ (B1) and $N(r)$ (B2); the latter is employed to estimate the uncertainty in $D3(r)$. As expected, larger flows decorrelate more slowly than small-scale flows (black solid); consequently, $N(r)$ decreases with r (red solid) (Fig. B1c).

This manuscript is a non-peer reviewed manuscript submitted to EarthArXiv.
This manuscript is under review for publication in Journal of Atmospheric and Oceanic Technology.
Copyright in this Work may be transferred without further notice.

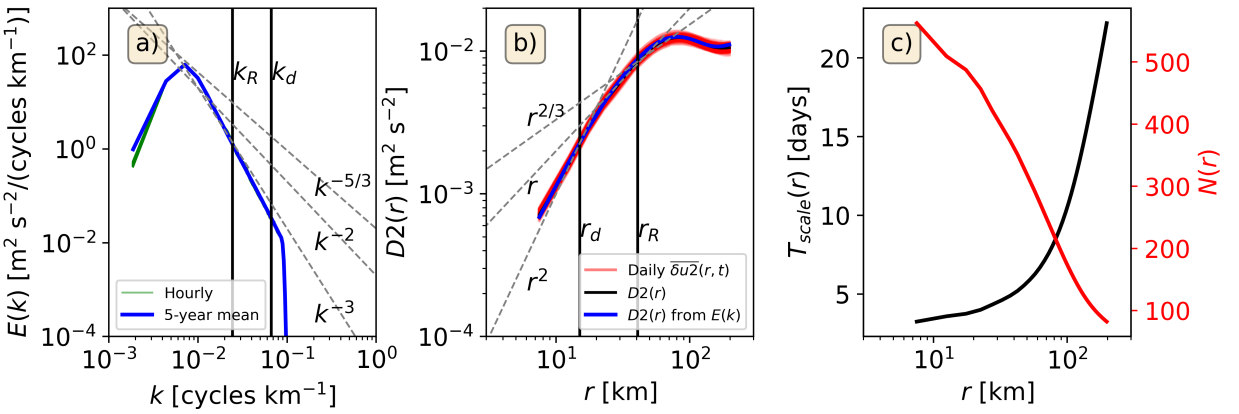

FIG. B1. (a) Upper-layer QG KE spectrum $E(k)$ [m^2 s^{-2}/(cycles km^{-1})]. Solid blue shows the 5-year mean spectrum using daily-averaged fields. Hourly spectra calculated for the last year of the model output are shown in green solid. Vertical solid lines show the model's Rhines wavenumber $k_R = \sqrt{\beta/U}$ and Rossby wavenumber $k_d = r_d^{-1}$, where r_d is the model's Rossby radius. (b) Second-order structure function $D2(r)$ [m^2 s^{-2}]. Red solid curves represent daily estimates $\overline{\delta u2}(r,t)$. Black and blue are the 5-year mean $D2(r)$ and the structure function estimated from the KE spectrum $D2(r)$ (5), respectively. Power laws for (a) and (b) are shown in dashed gray. Solid vertical lines show the model's r_d and Rhine's scale $r_R = 1/k_d$. (c) Decorrelation time scale $T_{scale}(r)$ [days] (black; left y-axis) and degrees of freedom $N(r)$ (red; right y-axis) estimated using (B1) and (B2), respectively and setting $T_{tot} = 5$ years.

Drifter data

Following Balwada et al. (2022), we estimated $D2(r)$ by replacing the ensemble averaging of $\delta u2(\mathbf{s},\mathbf{r},t)$ by averaging all samples per r bin to estimate $D2(r)$. Submesoscales with scales $r < 10^1$ km are more energetic during the winter (blue solid) than in summer (red solid), whereas mesoscales ($r \leq 10^1$ km) are more energetic during the summer than winter (Fig. B2a). The energizing of submesoscales in winter is likely driven by energetic submesoscale mixed layer instabilities that convert potential energy stored in the winter deep mixed layer to KE at the scales of the mixed layer deformation radius (Callies et al. 2015; Balwada et al. 2022). As in the model, $T_{scale}(r)$ increases linearly (in log-log space) with r where submesoscales for both seasons have shorter (< 1 day) time scales than mesoscales, with summertime (red solid) have slightly shorter $T_{scale}(r)$ at submesoscales than wintertime (blue solid) (Fig. B2b). $N(r)$ decreases with r with summertime (red solid) having slightly more $N(r)$ than wintertime (blue solid) (except for 10^-1

This manuscript is a non-peer reviewed manuscript submitted to EarthArXiv.
This manuscript is under review for publication in Journal of Atmospheric and Oceanic Technology.
Copyright in this Work may be transferred without further notice.

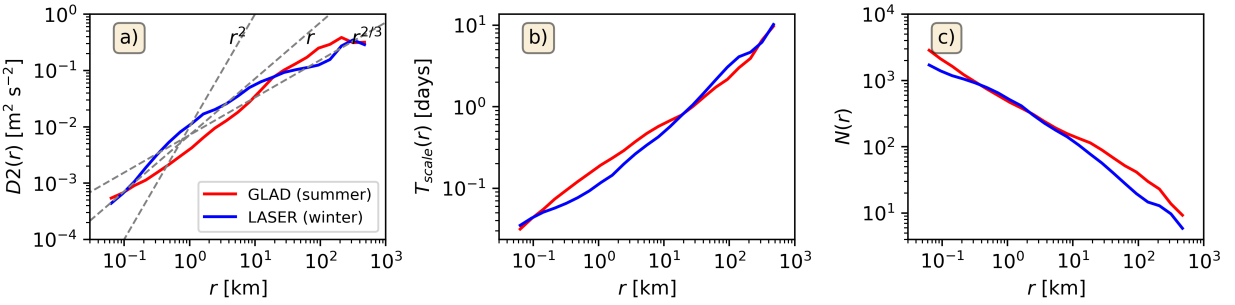

FIG. B2. (a) Second-order structure function $D2(r)$ [m^2 s^{-2}] for the GLAD (red solid) and LASER (blue solid) experiments. Power laws are shown in dashed gray. (b) Decorrelation time scale $T_{scale}(r)$ [days] (B1). (c) Degrees of freedom $N(r)$ (B2) estimated by setting $T_{tot} = 90$ days and 60 days for the GLAD and LASER experiments, respectively.

km $< r < 10^1$ km) as the GLAD experiment's duration is larger than that of the wintertime (Fig. B2.

APPENDIX C

First-order structure function

An important requirement for the structure-function theory is that the flow must be homogeneous, i.e., $D1(r) = 0$ for any length scale r (Frisch 1995). The mean current can determine the sign and magnitude of the $D3(r)$ limiting the application of the $D3(r)$ framework. In this appendix, we calculated $D1(r)$ from the velocity fields in the model and drifter data to analyze if the homogeneity condition is fulfilled.

Two-layer QG model

Daily $\overline{\delta u1}(r,t)$ is shown in Fig. C1a along with the five-year ensemble averaged $D1(r)$. The daily snapshots (orange solid) show relatively large variability for large r. The mean $D1(r)$ (black solid) is almost zero for $r < 60$ km but becomes statistically different from zero at the larger scales. The five-year mean longitudinal $D1_L(r)$ (blue solid) and transverse $D1_T(r)$ (red solid) structure-function components contribute equally to $D1(r)$.

This manuscript is a non-peer reviewed manuscript submitted to EarthArXiv.
This manuscript is under review for publication in Journal of Atmospheric and Oceanic Technology.
Copyright in this Work may be transferred without further notice.

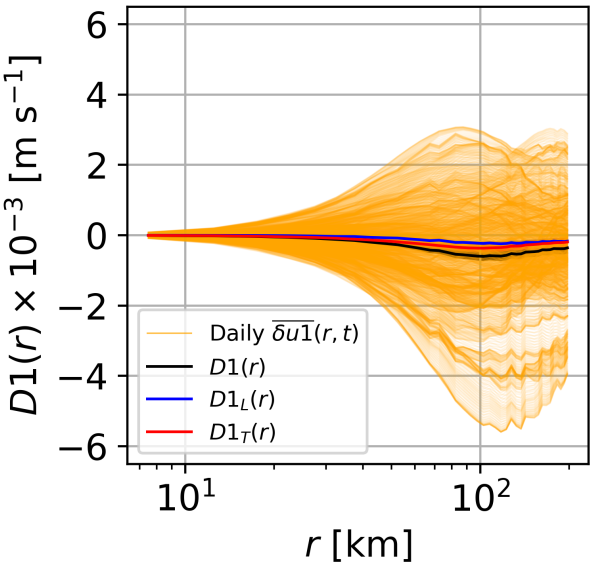

FIG. C1. Upper-layer fiver-year first-order structure function $D1(r)$ [m s^{-1}]. Orange lines are daily $\overline{\delta u1}(r,t)$. Black, blue, and red solid are the five-year ensemble averaged $D1$, longitudinal $D1_L(r)$ and transverse $D1_T(r)$ structure functions. Shaded gray, blue, and red correspond to their standard errors.

Drifter data

First-order structure function $D1(r)$ (Fig. C2a) for the GLAD (summer; red solid) and LASER (winter; blue solid) datasets show that the background flow has a large contribution across different flow scales, with a larger contribution at the mesoscales ($r \sim O(10^2)$ km) and during wintertime. Surface drifters converging into individual flow features such as mesoscale eddies and large-scale currents (Fig. 1) could result in highly heterogeneous sampling (Pearson et al. 2020). Skewness in both datasets shows that $\overline{\delta u1}(r,t)$ is slightly positively skewed for $r > 10^{-1}$ km (Fig. C2b). The high kurtosis relative to the mean for each r bin and season shows that data distribution has heavy tails at submesoscales and diminishes to $O(1)$ for $r \sim 10$ km (Fig. C2c).

References

Abernathey, R., and Coauthors, 2022: PyQG. Zenodo, doi:https://doi.org/10.5281/zenodo.6563667.

Ajayi, A., J. Le Sommer, E. P. Chassignet, J.-M. Molines, X. Xu, A. Albert, and W. Dewar, 2021: Diagnosing Cross-Scale Kinetic Energy Exchanges From Two Submesoscale Permitting

This manuscript is a non-peer reviewed manuscript submitted to EarthArXiv.
This manuscript is under review for publication in Journal of Atmospheric and Oceanic Technology.
Copyright in this Work may be transferred without further notice.

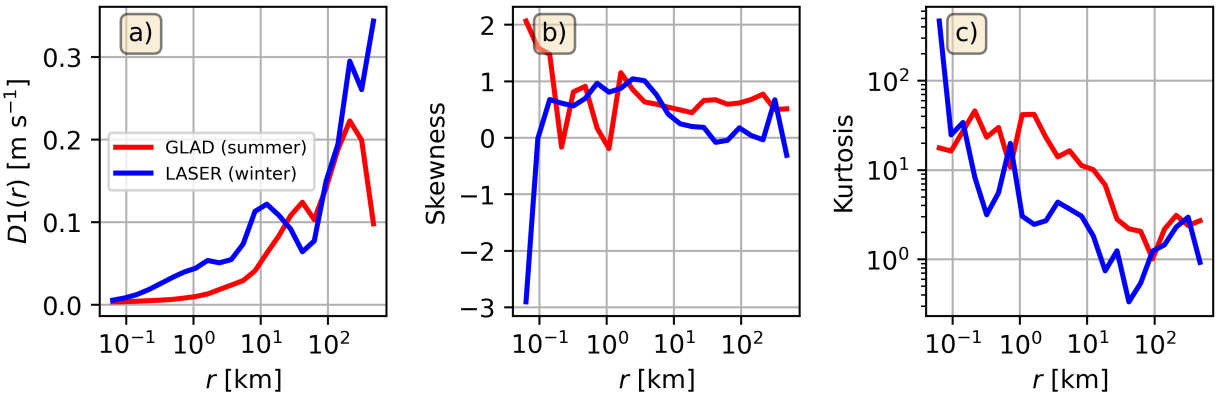

720 FIG. C2. (a) First-order structure function $D1(r)$ [m s^{-1}] for the GLAD (summer; red solid) and LASER
721 (winter; blue solid) experiments. (b) Skewness and (c) excess kurtosis of $\delta u1(\mathbf{s}, \mathbf{r}, t)$ for the GLAD and LASER
722 experiments.

728 Ocean Models. *Journal of Advances in Modeling Earth Systems*, **13 (6)**, e2019MS001 923,
729 doi:https://doi.org/10.1029/2019MS001923.

730 Aluie, H., M. Hecht, and G. K. Vallis, 2018: Mapping the energy cascade in the North Atlantic
731 Ocean: The coarse-graining approach. *Journal of Physical Oceanography*, **48 (2)**, 225 – 244,
732 doi:10.1175/JPO-D-17-0100.1.

733 Balwada, D., J. H. LaCasce, and K. G. Speer, 2016: Scale-dependent distribution of kinetic energy
734 from surface drifters in the gulf of mexico. *Geophysical Research Letters*, **43 (20)**, 10–856.

735 Balwada, D., Q. Xiao, S. Smith, R. Abernathey, and A. R. Gray, 2021: Vertical fluxes conditioned
736 on vorticity and strain reveal submesoscale ventilation. *Journal of Physical Oceanography*,
737 **51 (9)**, 2883–2901.

738 Balwada, D., J.-H. Xie, R. Marino, and F. Feraco, 2022: Direct observational evidence of an
739 oceanic dual kinetic energy cascade and its seasonality. *Science Advances*, **8 (41)**, eabq2566,
740 doi:10.1126/sciadv.abq2566.

741 Barndorff-Nielsen, O. E., P. Blæsild, and J. Schmiegel, 2004: A parsimonious and universal
742 description of turbulent velocity increments. *The European Physical Journal B-Condensed*
743 *Matter and Complex Systems*, **41 (3)**, 345–363, doi:https://doi.org/10.1140/epjb/e2004-00328-1.

**This manuscript is a non-peer reviewed manuscript submitted to EarthArXiv.
This manuscript is under review for publication in Journal of Atmospheric and Oceanic Technology.
Copyright in this Work may be transferred without further notice.**

Bennett, A. F., 1984: Relative dispersion: Local and nonlocal dynamics. *Journal of Atmospheric Sciences*, **41 (11)**, 1881 – 1886, doi:10.1175/1520-0469(1984)041⟨1881:RDLAND⟩2.0.CO;2.

Boccaletti, G., R. Ferrari, and B. Fox-Kemper, 2007: Mixed layer instabilities and restratification. *Journal of Physical Oceanography*, **37 (9)**, 2228 – 2250, doi:https://doi.org/10.1175/JPO3101.1.

Callies, J., R. Ferrari, J. M. Klymak, and J. Gula, 2015: Seasonality in submesoscale turbulence. *Nature communications*, **6 (1)**, 6862, doi:https://doi.org/10.1038/ncomms7862.

Capet, X., J. C. McWilliams, M. J. Molemaker, and A. F. Shchepetkin, 2008: Mesoscale to Submesoscale Transition in the California Current System. Part III: Energy Balance and Flux. *Journal of Physical Oceanography*, **38 (10)**, 2256 – 2269, doi:10.1175/2008JPO3810.1, URL https://journals.ametsoc.org/view/journals/phoc/38/10/2008jpo3810.1.xml.

Charney, J. G., 1971: Geostrophic Turbulence. *Journal of Atmospheric Sciences*, **28 (6)**, 1087 – 1095, doi:10.1175/1520-0469(1971)028⟨1087:GT⟩2.0.CO;2, URL https://journals.ametsoc.org/view/journals/atsc/28/6/1520-0469_1971_028_1087_gt_2_0_co_2.xml.

Cho, J. Y. N., and E. Lindborg, 2001: Horizontal velocity structure functions in the upper troposphere and lower stratosphere: 1. Observations. *Journal of Geophysical Research: Atmospheres*, **106 (D10)**, 10 223–10 232, doi:10.1029/2000JD900814.

DeMarco, A. W., and S. Basu, 2017: Estimating higher-order structure functions from geophysical turbulence time series: Confronting the curse of the limited sample size. *Physical Review E*, **95 (5)**, 052 114, doi:https://doi.org/10.1103/PhysRevE.95.052114.

Deusebio, E., P. Augier, and E. Lindborg, 2014: Third-order structure functions in rotating and stratified turbulence: a comparison between numerical, analytical and observational results. *Journal of fluid mechanics*, **755**, 294–313, doi:10.1017/jfm.2014.414.

Dong, J., B. Fox-Kemper, H. Zhang, and C. Dong, 2020: The seasonality of submesoscale energy production, content, and cascade. *Geophysical Research Letters*, **47 (6)**, e2020GL087 388, doi:https://doi.org/10.1029/2020GL087388.

Ferrari, R., and C. Wunsch, 2009: Ocean circulation kinetic energy: Reservoirs, sources, and sinks. *Annual Review of Fluid Mechanics*, **41 (1)**, 253–282.

This manuscript is a non-peer reviewed manuscript submitted to EarthArXiv.
This manuscript is under review for publication in Journal of Atmospheric and Oceanic Technology.
Copyright in this Work may be transferred without further notice.

Fox-Kemper, B., R. Ferrari, and R. Hallberg, 2008: Parameterization of Mixed Layer Eddies. Part I: Theory and Diagnosis. *Journal of Physical Oceanography*, **38 (6)**, 1145 – 1165, doi:10.1175/2007JPO3792.1, URL https://journals.ametsoc.org/view/journals/phoc/38/6/2007jpo3792.1.xml.

Freilich, M., L. Lenain, and S. T. Gille, 2023: Characterizing the role of non-linear interactions in the transition to submesoscale dynamics at a dense filament. *Geophysical Research Letters*, **50 (15)**, e2023GL103 745, doi:https://doi.org/10.1029/2023GL103745.

Frisch, U., 1995: *Turbulence: the legacy of AN Kolmogorov*. Cambridge university press.

Kachelein, L., B. D. Cornuelle, S. T. Gille, and M. R. Mazloff, 2022: Harmonic analysis of non-phase-locked tides with red noise using the red tide package. *Journal of Atmospheric and Oceanic Technology*, **39 (7)**, 1031 – 1051, doi:https://doi.org/10.1175/JTECH-D-21-0034.1.

Kolmogorov, A. N., 1991: The local structure of turbulence in incompressible viscous fluid for very large Reynolds numbers. *Proceedings of the Royal Society of London. Series A: Mathematical and Physical Sciences*, **434 (1890)**, 9–13.

Kunsch, H. R., 1989: The Jackknife and the Bootstrap for General Stationary Observations. *The Annals of Statistics*, **17 (3)**, 1217 – 1241, doi:10.1214/aos/1176347265, URL https://doi.org/10.1214/aos/1176347265.

Lindborg, E., 1999: Can the atmospheric kinetic energy spectrum be explained by two-dimensional turbulence? *Journal of Fluid Mechanics*, **388**, 259–288, doi:10.1017/S0022112099004851.

Lindborg, E., and J. Y. N. Cho, 2001: Horizontal velocity structure functions in the upper troposphere and lower stratosphere: 2. Theoretical considerations. *Journal of Geophysical Research: Atmospheres*, **106 (D10)**, 10 233–10 241, doi:https://doi.org/10.1029/2000JD900815.

Naveira Garabato, A. C., X. Yu, J. Callies, R. Barkan, K. L. Polzin, E. E. Frajka-Williams, C. E. Buckingham, and S. M. Griffies, 2022: Kinetic energy transfers between mesoscale and submesoscale motions in the open ocean's upper layers. *Journal of Physical Oceanography*, **52 (1)**, 75–97, doi:10.1175/JPO-D-21-0099.1.

This manuscript is a non-peer reviewed manuscript submitted to EarthArXiv.
This manuscript is under review for publication in Journal of Atmospheric and Oceanic Technology.
Copyright in this Work may be transferred without further notice.

Pearson, B. C., J. L. Pearson, and B. Fox-Kemper, 2021: Advective structure functions in anisotropic two-dimensional turbulence. *Journal of Fluid Mechanics*, **916**, A49, doi: 10.1017/jfm.2021.247.

Pearson, J., and Coauthors, 2020: Biases in structure functions from observations of submesoscale flows. *Journal of Geophysical Research: Oceans*, **125 (6)**, e2019JC015 769, doi:https://doi.org/10.1029/2019JC015769.

Poje, A. C., T. M. Özgökmen, D. J. Bogucki, and A. Kirwan, 2017: Evidence of a forward energy cascade and kolmogorov self-similarity in submesoscale ocean surface drifter observations. *Physics of Fluids*, **29 (2)**.

Qiu, B., T. Nakano, S. Chen, and P. Klein, 2022: Bi-directional energy cascades in the Pacific Ocean from equator to Subarctic Gyre. *Geophysical Research Letters*, **49 (8)**, e2022GL097 713, doi:10.1029/2022GL097713.

Ross, A., Z. Li, P. Perezhogin, C. Fernandez-Granda, and L. Zanna, 2023: Benchmarking of Machine Learning Ocean Subgrid Parameterizations in an Idealized Model. *Journal of Advances in Modeling Earth Systems*, **15 (1)**, e2022MS003 258, doi:https://doi.org/10.1029/2022MS003258.

Sasaki, H., P. Klein, Y. Sasai, and B. Qiu, 2017: Regionality and seasonality of submesoscale and mesoscale turbulence in the north pacific ocean. *Ocean Dynamics*, **67**, 1195–1216.

Schubert, R., J. Gula, R. J. Greatbatch, B. Baschek, and A. Biastoch, 2020: The Submesoscale Kinetic Energy Cascade: Mesoscale Absorption of Submesoscale Mixed Layer Eddies and Frontal Downscale Fluxes. *Journal of Physical Oceanography*, **50 (9)**, 2573 – 2589, doi:https://doi.org/10.1175/JPO-D-19-0311.1.

Schubert, R., O. Vergara, and J. Gula, 2023: The open ocean kinetic energy cascade is strongest in late winter and spring. *Communications Earth & Environment*, **4 (1)**, 450, doi:https://doi.org/10.1038/s43247-023-01111-x.

Scott, R. B., and F. Wang, 2005: Direct evidence of an oceanic inverse kinetic energy cascade from satellite altimetry. *Journal of Physical Oceanography*, **35 (9)**, 1650–1666.

Sheppard, K., and Coauthors, 2024: bashtage/arch: Release 7.0.0. Zenodo, URL https://doi.org/10.5281/zenodo.10981635, doi:10.5281/zenodo.10981635.

This manuscript is a non-peer reviewed manuscript submitted to EarthArXiv.
This manuscript is under review for publication in Journal of Atmospheric and Oceanic Technology.
Copyright in this Work may be transferred without further notice.

825 Srinivasan, K., R. Barkan, and J. C. McWilliams, 2023: A forward energy flux at submesoscales
826 driven by frontogenesis. *Journal of Physical Oceanography*, **53 (1)**, 87 – 305, doi:https://doi.
827 org/10.1175/JPO-D-22-0001.1.

828 Steinberg, J. M., S. T. Cole, K. Drushka, and R. P. Abernathey, 2022: Seasonality of the mesoscale
829 inverse cascade as inferred from global scale-dependent eddy energy observations. *Journal of*
830 *Physical Oceanography*, **52 (8)**, 1677–1691.

831 Storer, B. A., M. Buzzicotti, H. Khatri, S. M. Griffies, and H. Aluie, 2023: Global cascade of
832 kinetic energy in the ocean and the atmospheric imprint. *Science Advances*, **9 (51)**, eadi7420.

833 Stroock, D. W., 2010: *Probability theory: an analytic view*. Cambridge university press.

834 Tedesco, P. F., L. E. Baker, A. C. N. Garabato, M. R. Mazloff, S. T. Gille, C. P. Caulfield, and
835 A. Mashayek, 2024: Spatiotemporal Characteristics of the Near-Surface Turbulent Cascade
836 at the Submesoscale in the Drake Passage. *Journal of Physical Oceanography*, **54 (1)**, 187 –
837 215, doi:10.1175/JPO-D-23-0108.1, URL https://journals.ametsoc.org/view/journals/phoc/54/
838 1/JPO-D-23-0108.1.xml.

839 Uchida, T., Q. Jamet, A. C. Poje, N. Wienders, W. K. Dewar, and B. Deremble, 2023: Wavelet-
840 based wavenumber spectral estimate of eddy kinetic energy: Idealized quasi-geostrophic flow.
841 *Journal of Advances in Modeling Earth Systems*, **15 (3)**, e2022MS003 399.

842 Vallis, G. K., 2017: *Atmospheric and oceanic fluid dynamics*. Cambridge University Press.

843 Wunsch, C., 1996: *The Ocean Circulation Inverse Problem*. Cambridge University Press, Cam-
844 bridge, 437 pp.

845 Xie, J.-H., and O. Bühler, 2019: Third-order structure functions for isotropic turbulence with
846 bidirectional energy transfer. *Journal of Fluid Mechanics*, **877**, R3, doi:10.1017/jfm.2019.651.

847 Zhang, Z., and Coauthors, 2023: Submesoscale inverse energy cascade enhances southern ocean
848 eddy heat transport. *nature communications*, **14 (1)**, 1335.